

Object–vector coding in the medial entorhinal cortex

Øyvind Arne Høydal^{1*}, Emilie Ranheim Skytøen^{1,2}, Sebastian Ola Andersson^{1,2}, May-Britt Moser¹ & Edvard I. Moser^{1*}

The hippocampus and the medial entorhinal cortex are part of a brain system that maps self-location during navigation in the proximal environment^{1,2}. In this system, correlations between neural firing and an animal's position or orientation are so evident that cell types have been given simple descriptive names, such as place cells³, grid cells⁴, border cells^{5,6} and head-direction cells⁷. While the number of identified functional cell types is growing at a steady rate, insights remain limited by an almost-exclusive reliance on recordings from rodents foraging in empty enclosures that are different from the richly populated, geometrically irregular environments of the natural world. In environments that contain discrete objects, animals are known to store information about distance and direction to those objects and to use this vector information to guide navigation^{8–10}. Theoretical studies have proposed that such vector operations are

supported by neurons that use distance and direction from discrete objects^{11,12} or boundaries^{13,14} to determine the animal's location, but—although some cells with vector-coding properties may be present in the hippocampus¹⁵ and subiculum^{16,17}—it remains to be determined whether and how vectorial operations are implemented in the wider neural representation of space. Here we show that a large fraction of medial entorhinal cortex neurons fire specifically when mice are at given distances and directions from spatially confined objects. These 'object-vector cells' are tuned equally to a spectrum of discrete objects, irrespective of their location in the test arena, as well as to a broad range of dimensions and shapes, from point-like objects to extended surfaces. Our findings point to vector coding as a predominant form of position coding in the medial entorhinal cortex.

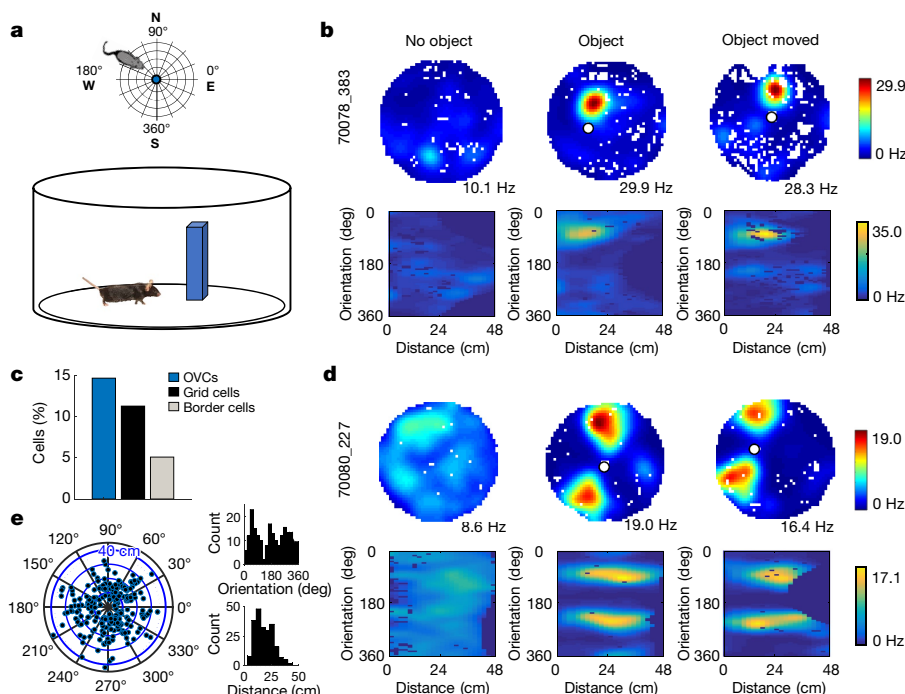


Fig. 1 | Object–vector cells fire at fixed distances and directions from objects. **a**, Schematics of recording environment (bird's-eye view and side view). Distance and direction (orientation) are defined in an allocentric frame with reference to the centre of the object (central circle). East is 0°. **b**, Top, colour-coded firing rate maps (with peak rates) showing an example cell that expressed a new firing field when an object (white circle) was introduced into the recording enclosure (middle). When the object was moved, the firing field moved accordingly (right). Mouse and cell identifier numbers are indicated (5 and 3 digits in length, respectively). Bottom, colour-coded vector maps showing firing rate for cell in top row as a function of distance (x-axis) and allocentric orientation (y-axis) from the centre of the object. Scale bar, colour-coded firing rate. The vector map for the non-object trial is referred to the object position on the first

object trial. **c**, Fractions of grid cells, object–vector cells (OVCs) and border cells in the entire population of recorded MEC cells. **d**, A subset of object–vector cells had two object–vector fields. Symbols as in **b**. **e**, Left, polar scatter plot showing orientation versus distance to object for all object–vector fields ($n = 162$ cells, 16 mice). Orientation (polar axis) and distance (radial axis, 40 cm indicated in blue) are defined by the centre of mass of the object–vector field in the vector map. Top right, frequency distribution showing orientation for all fields in the vector map that were stable between object and displaced-object trials. Bottom right, frequency distribution showing distance (object perimeter to field centre) for the same fields (median 17.0 cm; 25–75th percentiles 12.0–24.3 cm; maximum 43.1 cm).

¹Kavli Institute for Systems Neuroscience and Centre for Neural Computation, Norwegian University of Science and Technology (NTNU), Trondheim, Norway. ²These authors contributed equally: Emilie Ranheim Skytøen, Sebastian Ola Andersson. *e-mail: oyvind.a.hoydal@ntnu.no; edvard.moser@ntnu.no

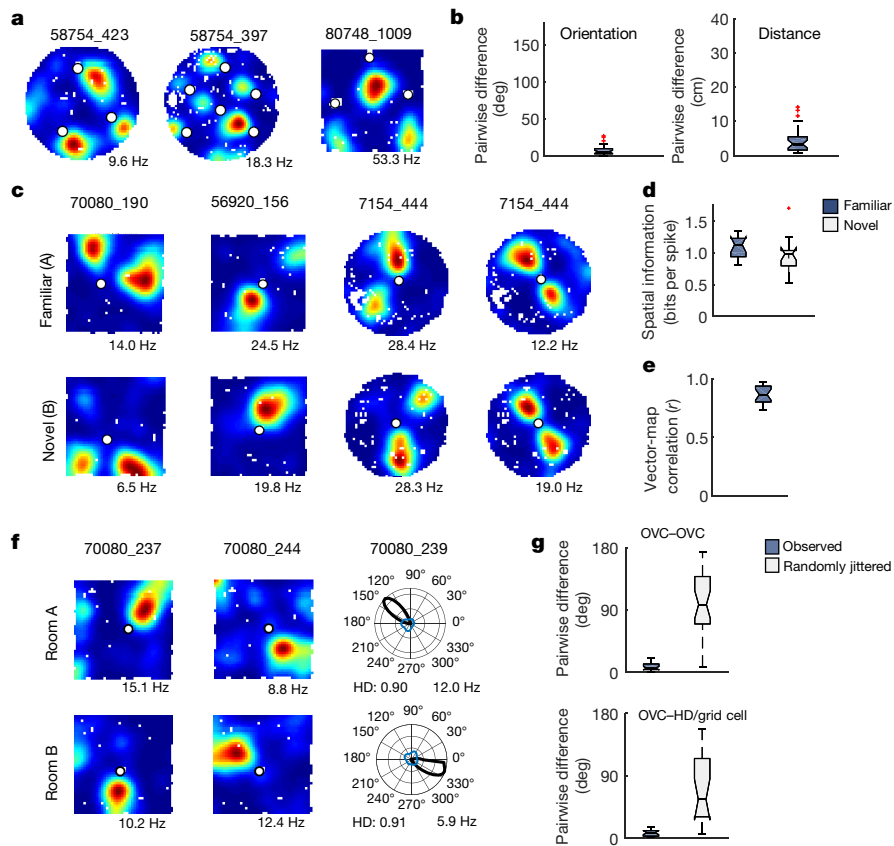


Fig. 2 | Object-vector cells generalize between objects and environments. **a**, Firing rate maps for three cells recorded with either three or six objects in the box. **b**, Differences in orientation (left) and distance (right) from the object for all pairs of object-vector fields in the same experiment ($n = 23$ cells, 7 mice, median orientation 5.8° (25th–75th percentiles 3.3° – 10.2°); median distance 3.4 cm (1.7– 5.5 cm)). Line between box edges, median; box edges, 25th and 75th percentiles; whiskers, points within 1.5 times the interquartile range; red crosses, outliers (applies to all box plots). **c**, Colour-coded rate maps for four example cells recorded in familiar environment A (top) and novel environment B with a novel object (bottom). **d**, Spatial information for all cells recorded successively in familiar and novel environments ($n = 14$ cells, 4 mice; familiar median 1.13 bits per spike (0.94–1.23 bits per spike); novel median 0.99 bits per spike (0.80–1.03 bits per spike); two-sided Wilcoxon signed rank test, $W = 77$, $n = 14$, $P = 0.14$). **e**, Vector-map

correlation between rooms A and B for all cells recorded in both rooms ($n = 20$ cells, 5 mice; median $r = 0.87$ (0.80–0.94)). **f**, Firing rate maps for two object-vector cells and directional tuning curve for one head-direction cell recorded concurrently in rooms A (top) and B (bottom). Peak rate (Hz) and head-direction score (HD) are indicated. **g**, Top, difference in orientation between rooms A and B for all pairs of simultaneously recorded object-vector cells compared to differences between these pairs when orientation tuning curves were randomly shifted ($n = 20$ cells; observed median 6° (4° – 12°); jittered median 98° (70° – 138.5°); two-sided Wilcoxon signed rank test, $W = 0$, $P = 2.6 \times 10^{-6}$). Bottom, as in top panel but for pairs consisting of an object-vector cell and a head-direction or grid cell ($n = 18$ object-vector cells, 5 head-direction cells, 2 grid cells; observed median 6° (3° – 11°); jittered median 56° (31° – 115°); $W = 3.5$, $P = 1.5 \times 10^{-4}$).

Natural environments contain objects, and animals may use these to map locations. In the lateral entorhinal cortex^{18,19} and areas connected with it^{20,21}, subsets of cells fire specifically when animals encounter discrete objects in an otherwise-open environment. But how representations of objects are used to navigate in the space between objects remains to be determined. Here we searched for object-guided representations of space in superficial layers of the medial entorhinal cortex (MEC) (Extended Data Fig. 1), a brain region that is characterized by accurate position coding in specialized cell types^{4–7,22,23}. Cells were recorded while mice foraged in square or circular arenas with one or several prism or cylinder-shaped objects placed on the floor of the compartment (Fig. 1a, Extended Data Fig. 2; 1,100 cells, 16 mice). When a discrete object was present, many MEC cells encoded the mouse's allocentric direction (orientation) and distance from this object, in a vector-like manner (Fig. 1b–d, Extended Data Fig. 3).

We first investigated whether activity in MEC cells was changed by the introduction of an object (Fig. 1b). On trial 1 of the experiment, there was no object. On trial 2, an object was put on the floor, and on trial 3, the object was moved to a different location. On trial 2, many MEC cells developed firing fields. These fields were mostly offset from the object, often by several tens of centimetres, and for the majority of

cells, displacements from the object were retained on trial 3, as if they encoded an allocentric vector from the object (Fig. 1b, d).

To explore this possibility, we first identified cells with significant spatial information on trial 2 (bits per spike exceeding the 95th percentile of a distribution of spatial information values in shuffled data, $n = 460$) and then selected the subset of cells in this sample that expressed new firing fields when the object was introduced ($n = 205$). For all selected cells in which firing fields were displaced from the object (object-field distance more than 4 cm; 202 cells), we constructed vector maps that expressed firing rate as a function of distance and direction from the centre of the object (Fig. 1b, bottom, Supplementary Text). A cell was categorized as an object-vector cell if the correlation of vector maps on trials 2 and 3 (with objects in different locations) exceeded the 99th percentile value ($r = 0.42$) of a distribution of correlation values in shuffled data. In total, 162 cells passed this criterion. In the total sample of 1,100 cells, the proportion of object-vector cells (14.7%) exceeded that of grid cells (11.3%) and border cells (5.1%) (Fig. 1c). Very few object-vector cells satisfied the criteria for other cell types (Extended Data Fig. 4). Of the object-vector cells, 106 (65%) had one object-induced field; 53 (33%) had two, and 3 (2%) had three (Fig. 1d, Extended Data Fig. 5). The firing fields were always encoded

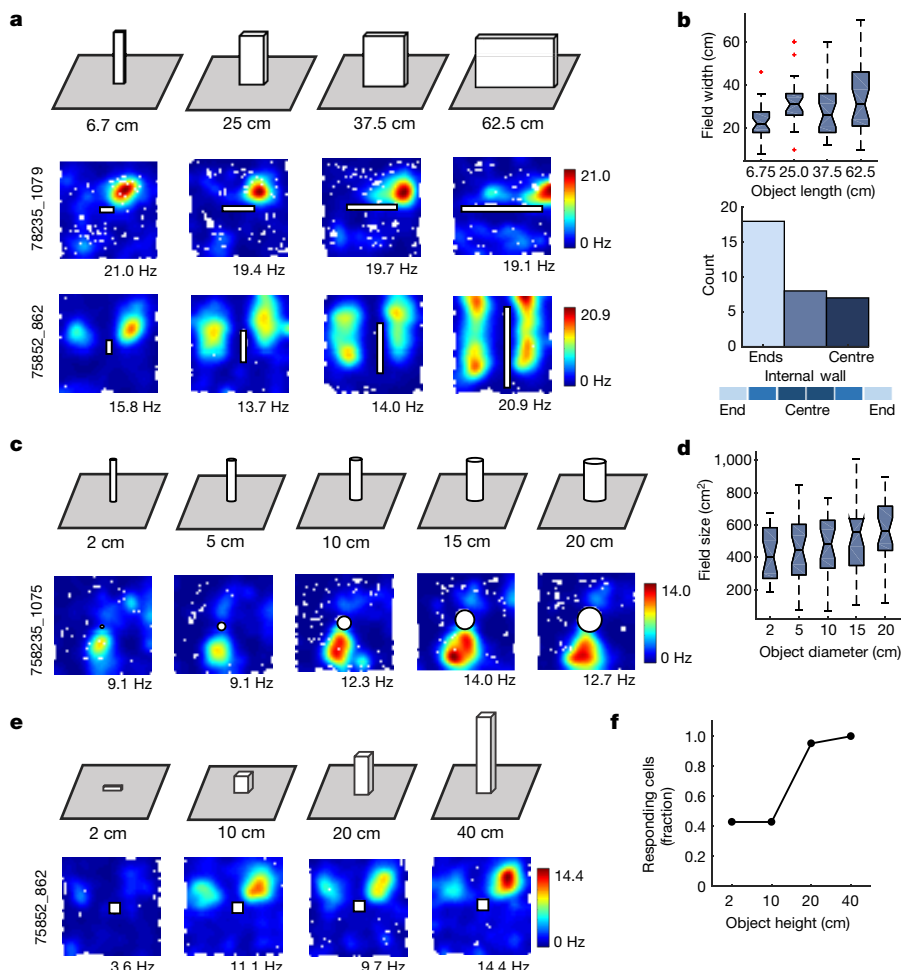


Fig. 3 | Vector encoding is retained across a broad range of object shapes and sizes. **a**, Response of object-vector cells to increased length of a prismatic object. Top, experimental procedure. Middle, colour-coded firing rate maps for an example cell. The cell retained a similarly sized firing field across all conditions. Bottom, corresponding firing rate maps for a different cell. In this cell, the length of the firing fields increased in parallel with the length of the object. Local peaks formed at both ends of the longest firing fields. **b**, Top, distribution of field widths for all object-vector cells recorded with elongated prism objects. Note the greater spread for the widest object ($n = 24$ cells, 5 mice, Kruskal–Wallis test, $H = 12.03$, $P = 0.007$). Bottom, distribution of locations on the internal wall for which the vector to the peak of a firing field was most similar to the object-vector on a trial with a point-like object. Note over-representation of the edges (goodness of fit against uniform distribution, $\chi^2 = 6.7$, $P = 0.035$). **c**, Firing rate maps showing response of object-vector cells to increased diameter of a cylindrical object. **d**, Distribution of field sizes for all object-vector cells recorded with increasing cylinder diameter ($n = 23$ cells, 5 mice). **e**, Firing rate maps showing response of object-vector cells to increased height of a prismatic object. **f**, Fraction of object-vector cells responding to the four object heights ($n = 21$ cells, 6 mice).

in an allocentric framework—that is, independently of the mouse’s direction of movement relative to the object (Extended Data Fig. 6). This clearly distinguishes object-vector cells from cells in the lateral entorhinal cortex and hippocampus that encode object bearings with an egocentric reference^{24,25}. The allocentric orientations of the object-vector fields covered the entire azimuthal range and a wide span of distances (Fig. 1e).

Object-vector cells have properties in common with ‘landmark-vector cells’ in hippocampal area CA1¹⁵. Landmark-vector cells differentiate between subsets of objects, much as place cells remap between contexts and environments²⁶. To determine whether similar specificity is present in object-vector cells in the MEC, we introduced 2–6 distinct objects into the box (Extended Data Fig. 2a, b). In 51 of 52 object-cell pairs, firing fields emerged in response to the objects (Fig. 2a, b). Pairwise differences in distance and orientation from objects to fields were small (Fig. 2b), which suggests that object-vector cells in the MEC fire at similar displacements across objects.

Another property of CA1 landmark-vector cells is their slow emergence and apparent dependence on experience¹⁵. We investigated whether object-vector cells in the MEC require similarly extended or repeated experience. Object-vector cells were recorded in a familiar

room (A) and in a novel or less-familiar room (B). Fourteen of the cells were recorded during the mouse’s first exposure to room B. Both the box and the objects were novel. All cells with object-vector fields in A had also vector fields in B. Rate maps recorded in A and B had similar spatial information content (Fig. 2d), which suggests that object-vector cells are sharply tuned from the first trial with a novel object or environment. When vector maps in rooms A and B were rotated to maximize orientation similarity, the correlations between the vector maps became high (Fig. 2e), which suggests that the cells maintained their distance metrics across environments.

We then investigated whether ensembles of object-vector cells maintained their spatial relationships between the two environments, mirroring the fixed tuning relationships reported for grid cells²⁷ and head-direction cells²⁸. Pairs of simultaneously recorded object-vector cells maintained their orientation relationships across rooms. Differences in orientation shifts for simultaneously recorded cell pairs were significantly smaller than for randomly shifted orientation tuning curves (Fig. 2f, g, $P = 2.6 \times 10^{-6}$). Cell pairs consisting of one object-vector cell and one head-direction or grid cell showed similar coherence across environments (Fig. 2g). Orientation preferences were maintained between square and circular compartments (Extended Data

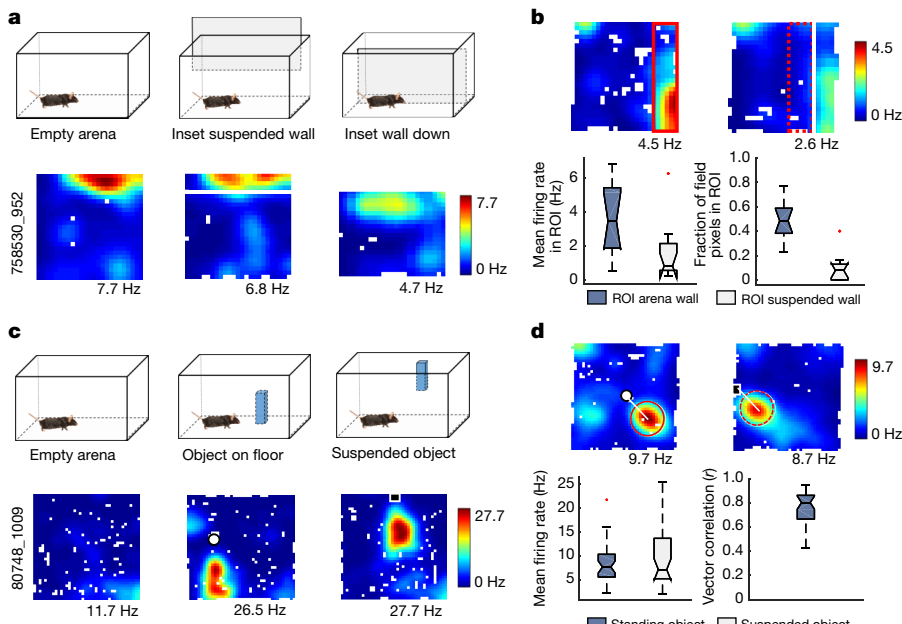


Fig. 4 | Border cells and object-vector cells encode different features of objects. **a**, Top row, experimental procedure. Bottom row, colour-coded firing rate maps for a representative border cell recorded with suspended wall and the same wall lowered to ground level. The cell did not produce a border field near the suspended wall but fired robustly when the wall obstructed the path of the mouse. **b**, Top, colour-coded rate maps showing ROIs for arena wall (left) and suspended wall (right). Bottom, distributions of mean firing rates (left), and fractions of bins exceeding threshold for firing fields (right), in ROIs. Mean firing rates and fractions were significantly lower along the suspended wall ($n = 11$ cells, 6 mice; median firing rate with suspended wall 0.83 Hz (25th–75th percentile 0.56–2.14 Hz); median peripheral wall 3.5 Hz (1.9–5.4 Hz), two-sided

Wilcoxon signed rank test, $W = 65, P = 0.002$; median fraction of bins with suspended wall: 0.08 (0–0.13); median standing wall 0.49 (0.38–0.59); $W = 66, P = 9.8 \times 10^{-4}$). **c**, Object-vector cells respond to objects independently of path obstruction. Top, experimental procedure. Bottom, firing rate maps of cell recorded with standing and suspended objects. **d**, Top, object-vector fields are similar for standing and suspended objects. Bottom, left, mean firing rates in ROIs for standing and suspended objects ($n = 32$ cells, 10 mice; median suspended object 7.1 Hz (5.2–13.7 Hz); median standing object 7.8 Hz (5.6–10.3 Hz); two-sided Wilcoxon signed rank test, $W = 204, P = 0.07$). Bottom, right, correlations of vector maps for the same pairs of trials. Correlations were significant for all cells ($n = 32$ cells, median $r = 0.80$ (0.67–0.86)).

Fig. 7a–c). Together, these observations suggest that a fixed directional structure was expressed across cell types in the MEC, independently of experience.

Vector coding has previously been described in the subiculum^{16,17}, where ‘boundary-vector cells’ fire at specific distances from specifically oriented environmental boundaries. Whereas cells with such properties are scarce in the MEC (Extended Data Fig. 8c, d, Supplementary Text), object-vector cells are abundant (Fig. 1c). This notable contrast led us to investigate which shapes of objects are encoded by object-vector cells. We recorded activity from object-vector cells while the length of a prismatic tower was changed in steps from 6.75 cm to 62.5 cm or vice versa (Fig. 3a, b, Extended Data Fig. 9a). Object-vector cells maintained firing fields at every length of the prism in 92 out of 96 instances. Some cells maintained a similar field size across all object lengths (Fig. 3a, cell 1,079); in others, the field was stretched as the length increased, sometimes splitting into discrete subfields near the ends of the object (Fig. 3a, cell 862, Extended Data Fig. 9a). For the cell sample as a whole, there was a significant effect of object length on the length of the firing fields (Fig. 3b, top, $P = 0.007$). Firing fields were anchored more frequently to the ends of the elongated object than to any other location on it (Fig. 3b, bottom). Peak and mean firing rates did not change (Supplementary Text).

In similar parametric experiments, we changed the diameter of a cylindrical object and the height of a prism. Object-vector cells maintained firing fields at similar distances and directions from the perimeter of the cylinder irrespective of diameter (mean vector map correlation across all conditions for all cells: 0.80 ± 0.001 , mean \pm s.e.m.). There was no significant effect of object size on the size of firing fields (Fig. 3c, d). The cells also responded to a wide range of prism heights, although there was a preference for taller objects. Only 43% of the cells expressed object-vector fields with the 2-cm-high object. Together, these observations demonstrate discrete firing fields

in the presence of a broad spectrum of object identities and shapes, including both point-like and elongated structures.

In a final set of experiments, we tested whether object-vector cells could be distinguished from border cells^{5,6}. Border cells may represent one end of a continuum of object- or boundary-vector-encoding cells with offsets so short that the fields encroach on the defining wall, or they may encode entirely different task features, such as obstruction of the animal’s path. To address this, we inserted a wall and lifted it 15 cm above the floor, enough to not impede the mouse’s trajectory. Border cells generally failed to produce a border field along the suspended wall, but responded robustly when the same wall was lowered to the ground, obstructing the mouse’s path (Fig. 4a, Supplementary Text). To quantify this difference, we defined comparable rectangular regions of interest (ROIs) along the peripheral and suspended walls (Fig. 4b, top). Mean firing rates and fractions of active spatial bins were substantially lower in the ROI along the suspended wall (Fig. 4b, bottom), which suggests that blockade of the mouse’s trajectory is a major factor that contributes to firing in border cells.

To test whether path obstruction also accounted for firing in object-vector cells, we lifted objects 15 cm above the floor (Fig. 4c). In 32 out of 32 object-vector cells tested in this way, firing fields were evoked with the suspended object (Fig. 4c, Extended Data Fig. 10). To compare responses to standing and suspended objects, we defined ROIs with similar vector relationships to the reference object (Fig. 4d, top). Within ROIs, mean firing rates were not significantly different (Fig. 4d, bottom). Vector-map correlations between suspended and standing object trials were high for all cells (Fig. 4d). Thus, in contrast to border fields, object-vector fields are elicited independently of whether the object affects the mouse’s trajectory.

Together, our findings indicate that allocentric vector coding is a predominant form of position coding in superficial layers of the MEC, distinct from the vectorial representations reported previously in the

hippocampus and subiculum (Supplementary Text). A substantial proportion of MEC cells discharged at specific distances and directions from salient objects, independently of the identity, size or location of the object or the orientation of the mouse's body axis. Discrete high-contrast objects induced object-vector fields regardless of whether they were internal to the environment or attached to external bounding walls. Object-vector cells intermingled with grid cells and head-direction cells that encode position in a distal framework^{4,6,22}. The various cell types remained aligned with each other across environments, which suggests that they are part of a single interconnected, low-dimensional network for representation of location^{27,29,30}.

Object-vector cells are distinct from object cells in the lateral entorhinal cortex and associated areas^{18–21}, which respond only when the animal is at the object and not when it perceives it from a distance. Unlike object cells, object-vector cells provide a cellular basis for position mapping in the space between objects. Because animals use stable landmarks as references for navigation^{8–10}, theoretical studies have proposed the existence, in cortical networks, of allocentric vectorial representations that animals may use to infer position and trajectories to goals^{11–14}. The present study provides evidence for such object-related vectorial representations in the MEC.

Online content

Any methods, additional references, Nature Research reporting summaries, source data, statements of data availability and associated accession codes are available at <https://doi.org/10.1038/s41586-019-1077-7>.

Received: 5 March 2018; Accepted: 28 February 2019;

Published online: 03 April 2019

- O'Keefe, J. & Nadel, L. *The Hippocampus as a Cognitive Map* (Oxford Univ. Press, Oxford, 1978).
- Moser, E. I., Kropff, E. & Moser, M. B. Place cells, grid cells, and the brain's spatial representation system. *Annu. Rev. Neurosci.* **31**, 69–89 (2008).
- O'Keefe, J. & Dostrovsky, J. The hippocampus as a spatial map. Preliminary evidence from unit activity in the freely-moving rat. *Brain Res.* **34**, 171–175 (1971).
- Hafting, T., Fyhn, M., Molden, S., Moser, M. B. & Moser, E. I. Microstructure of a spatial map in the entorhinal cortex. *Nature* **436**, 801–806 (2005).
- Savelli, F., Yoganarasimha, D. & Knierim, J. J. Influence of boundary removal on the spatial representations of the medial entorhinal cortex. *Hippocampus* **18**, 1270–1282 (2008).
- Solstad, T., Boccara, C. N., Kropff, E., Moser, M. B. & Moser, E. I. Representation of geometric borders in the entorhinal cortex. *Science* **322**, 1865–1868 (2008).
- Taube, J. S., Müller, R. U. & Ranck, J. B. Jr. Head-direction cells recorded from the postsubiculum in freely moving rats. I. Description and quantitative analysis. *J. Neurosci.* **10**, 420–435 (1990).
- Collett, T. S., Cartwright, B. A. & Smith, B. A. Landmark learning and visuo-spatial memories in gerbils. *J. Comp. Physiol. A* **158**, 835–851 (1986).
- Biegler, R. & Morris, R. G. Landmark stability is a prerequisite for spatial but not discrimination learning. *Nature* **361**, 631–633 (1993).
- Hurly, T. A., Fox, T. A., Zwueste, D. M. & Healy, S. D. Wild hummingbirds rely on landmarks not geometry when learning an array of flowers. *Anim. Cogn.* **17**, 1157–1165 (2014).
- McNaughton, B. L., Knierim, J. J. & Wilson, M. A. in *The Cognitive Neurosciences* (ed. M.S. Gazzaniga) 585–595 (MIT Press, 1995).
- Stemmler, M., Mathis, A. & Herz, A. V. Connecting multiple spatial scales to decode the population activity of grid cells. *Sci. Adv.* **1**, e1500816 (2015).
- O'Keefe, J. & Burgess, N. Geometric determinants of the place fields of hippocampal neurons. *Nature* **381**, 425–428 (1996).
- Burgess, N., Jackson, A., Hartley, T. & O'Keefe, J. Predictions derived from modelling the hippocampal role in navigation. *Biol. Cybern.* **83**, 301–312 (2000).
- Deshmukh, S. S. & Knierim, J. J. Influence of local objects on hippocampal representations: landmark vectors and memory. *Hippocampus* **23**, 253–267 (2013).

- Barry, C. et al. The boundary vector cell model of place cell firing and spatial memory. *Rev. Neurosci.* **17**, 71–97 (2006).
- Lever, C., Burton, S., Jeewajee, A., O'Keefe, J. & Burgess, N. Boundary vector cells in the subiculum of the hippocampal formation. *J. Neurosci.* **29**, 9771–9777 (2009).
- Deshmukh, S. S. & Knierim, J. J. Representation of non-spatial and spatial information in the lateral entorhinal cortex. *Front. Behav. Neurosci.* **5**, 69 (2011).
- Tsao, A., Moser, M. B. & Moser, E. I. Traces of experience in the lateral entorhinal cortex. *Curr. Biol.* **23**, 399–405 (2013).
- Deshmukh, S. S., Johnson, J. L. & Knierim, J. J. Perirhinal cortex represents nonspatial, but not spatial, information in rats foraging in the presence of objects: comparison with lateral entorhinal cortex. *Hippocampus* **22**, 2045–2058 (2012).
- Weible, A. P., Rowland, D. C., Monaghan, C. K., Wolfgang, N. T. & Kentros, C. G. Neural correlates of long-term object memory in the mouse anterior cingulate cortex. *J. Neurosci.* **32**, 5598–5608 (2012).
- Sargolini, F. et al. Conjunctive representation of position, direction, and velocity in entorhinal cortex. *Science* **312**, 758–762 (2006).
- Kropff, E., Carmichael, J. E., Moser, M. B. & Moser, E. I. Speed cells in the medial entorhinal cortex. *Nature* **523**, 419–424 (2015).
- Sarel, A., Finkelstein, A., Las, L. & Ulanovsky, N. Vectorial representation of spatial goals in the hippocampus of bats. *Science* **355**, 176–180 (2017).
- Wang, C. et al. Egocentric coding of external items in the lateral entorhinal cortex. *Science* **362**, 945–949 (2018).
- Muller, R. U. & Kubie, J. L. The effects of changes in the environment on the spatial firing of hippocampal complex-spike cells. *J. Neurosci.* **7**, 1951–1968 (1987).
- Fyhn, M., Hafting, T., Treves, A., Moser, M. B. & Moser, E. I. Hippocampal remapping and grid realignment in entorhinal cortex. *Nature* **446**, 190–194 (2007).
- Yogararasimha, D., Yu, X. & Knierim, J. J. Head direction cell representations maintain internal coherence during conflicting proximal and distal cue rotations: comparison with hippocampal place cells. *J. Neurosci.* **26**, 622–631 (2006).
- Gardner, R. J., Lu, L., Wernle, T., Moser, M. B. & Moser, E. I. Correlation structure of grid cells is preserved during sleep. *Nat. Neurosci.* (in the press) (2019).
- Trettel, S. G., Trimper, J. B., Hwaun, E., Fiete, I. R. & Colgin, L. L. Grid cell co-activity patterns during sleep reflect spatial overlap of grid fields during active behaviors. *Nat. Neurosci.* (in the press) (2019).

Acknowledgements We thank A. M. Amundsgård, K. Haugen, K. Jenssen, V. Frolov, I. U. Kruse, N. Dagslott, E. Kråkvik and H. Waade for technical assistance. The work was supported by two Advanced Investigator Grants from the European Research Council (GRIDCODE, Grant Agreement N°338865; ENSEMBLE – Grant Agreement N°268598), a NEVRONOR grant from the Research Council of Norway (grant no. 226003), the Centre of Excellence scheme and the National Infrastructure Scheme of the Research Council of Norway (Centre for Neural Computation, grant number 223262; NORBRAIN1, grant number 197467), the Louis Jeantet Prize, the Körber Prize and the Kavli Foundation.

Reviewer information *Nature* thanks Martin Stemmler and the other anonymous reviewer(s) for their contribution to the peer review of this work.

Author contributions Ø.A.H., M.-B.M. and E.I.M. designed most experiments and analytic approaches; Ø.A.H., E.R.S. and S.O.A. collected data; Ø.A.H. performed analyses; M.-B.M. and E.I.M. supervised the project; Ø.A.H. and E.I.M. wrote the paper with input from all authors.

Competing interests The authors declare no competing interests.

Additional information

Extended data is available for this paper at <https://doi.org/10.1038/s41586-019-1077-7>.

Supplementary information is available for this paper at <https://doi.org/10.1038/s41586-019-1077-7>.

Reprints and permissions information is available at <http://www.nature.com/reprints>.

Correspondence and requests for materials should be addressed to Ø.A.H. or E.I.M.

Publisher's note: Springer Nature remains neutral with regard to jurisdictional claims in published maps and institutional affiliations.

© The Author(s), under exclusive licence to Springer Nature Limited 2019

METHODS

Subjects. Data were obtained from 16 male wild-type C57/BL6 mice aged 4–11 months. All mice were kept on a 12 h light/12 h dark schedule in a humidity and temperature-controlled environment. The mice were housed in single mouse cages after implantation. Testing occurred in the dark phase. The mice were not deprived of food or water. Experiments were performed in accordance with the Norwegian Animal Welfare Act and the European Convention for the Protection of Vertebrate Animals used for Experimental and Other Scientific Purposes.

Surgery and electrode implantation. The mice were anaesthetized with 5% isoflurane (air flow: 1.2 l/min) in an induction chamber. Upon induction of anaesthesia, they received subcutaneous injections of buprenorphine (Temgesic) and meloxicam (Metacam). The mice were then fixed in a Kopf stereotaxic frame for implantation. The local anaesthetic bupivacaine (Marcaine) was injected subcutaneously before the incision was made. During surgery, isoflurane was gradually reduced from 3% to 1% according to physiological condition. The depth of anaesthesia was monitored by testing tail and pinch reflexes as well as breathing.

Anaesthetized mice were implanted with a single bundle of four tetrodes attached to a microdrive fastened to the skull of the mouse. The tetrodes were targeted to the MEC at an angle of 3–4° relative to the bregma/lambda horizontal reference plane, with the tips pointing in the posterior direction. The tetrodes were inserted 3.1–3.3 mm lateral to the midline and 0.2–0.4 mm anterior to the transverse sinus edge, with an initial depth of 800 µm. The implant was secured to the skull with histocrylic and dental cement. One screw was connected to the drive ground.

Tetrodes were constructed from four twisted 17-µm polyimide-coated platinum-iridium (90–10%) wires (California Fine Wire). The electrode tips were plated with platinum to reduce electrode impedances to between 120 and 220 kΩ at 1 kHz. **Behavioural procedures.** The mice were trained to forage for cookie crumbs in an 80 cm × 80 cm square and a 90-cm-diameter circular compartment, both enclosed by 50-cm-high walls. A few experiments were conducted in a 100 cm × 100 cm square or a 65-cm-diameter circular compartment. Thick dark blue curtains surrounded the recording arena, except for a slit to one side. Before testing, the mouse rested outside the curtain in a plexiglass cage coated with towels. Testing was performed at low light levels to encourage exploration. Between trial sequences, the mat covering the floor of the recording box was cleaned.

The standard trial sequence started with a trial in which no object was present in the arena, followed by one in which a tower-shaped object (one of those shown in Extended Data Fig. 2a, b) was placed at a semi-randomly varied location, with a bias towards the box centre on the first trial (to capture fields with large offsets from the object). To verify that any observed change in neural activity between the first and the second trials was tied to the location of the object, the object was displaced in a pseudo-random fashion on a third trial in the sequence (only in those experiments in which object-responsive cells were present on the preceding trial). Trials were typically spaced by a few minutes, during which the experimenter clustered and inspected recorded cells and placed the object in a new location. The identity of the object used for standard trials was kept constant from day to day.

Parametric experiments were conducted to determine the range of object sizes and dimensions represented by object-vector cells. In one set of experiments, the object was extended in discrete steps along one dimension. Lego Duplo bricks were tethered together to form 21-cm-high, 3-cm-wide prismatic towers with lengths of 6.75 cm, 25 cm, 37.5 cm and 62.5 cm (Extended Data Fig. 2c). Cells were recorded in a sequence of four trials during which the length of the object increased for each trial in the sequence 6.75 cm, 25 cm, 37.5 cm and 62.5 cm. In some recordings, the sequence was reversed, starting with 62.5 cm and ending with 6.75 cm. In a second set of experiments, cells were recorded in a sequence of five trials in which the diameter of a cylindrical tower object was changed in incremental steps in the sequence 2 cm, 5 cm, 10 cm, 15 cm and 20 cm. Objects used in this experiment were made of paper (Extended Data Fig. 2d). The third set of parametric experiments tested the effect of object heights on object-vector responses. In a sequence of four trials, the height of a prismatic object was changed in incremental steps in the sequence 2 cm, 10 cm, 20 cm and 40 cm. The objects used for this experiment were Duplo bricks stacked on top of each other to create objects of different heights (Extended Data Fig. 2e).

To test whether object-vector cells generalize between object identities, cells were recorded in the presence of multiple objects (2–6, usually 2 or 3). Objects were selected from a pool of tower-like modified rectangular prisms or cylinders ranging in size between 3 and 7 cm in width and 9 and 20 cm in height for the prisms and between 3 and 8 cm in diameter and 20 and 35 cm in height for the cylinders (Extended Data Fig. 2a, b).

In another subset of tests, cells were recorded in two rooms—one familiar and one new to the mouse. A few cells were also recorded in both rooms after the initial test in the second room. In the novel condition, only novel objects were presented. The recording box was also novel. Both novel and familiar objects were chosen

from the pool of objects shown in Extended Data Fig. 2a, b. Tests in familiar and novel rooms were consecutive, with an interval of 10–15 min for transport and preparation. During preparation for recording, the mouse rested in a towel-coated plexiglass box on a pedestal outside the curtains.

In experiments with suspended objects, the object was taped to the wall with the lower end approximately 15 cm above the floor level. In a variant of this experiment, the object was attached to a suspended wall to dissociate the object from any surrounding obstruction. In each individual experiment, the mouse was observed to make sure the elevation was sufficient to not obstruct its movement in any way. Likewise, border cells were recorded in the presence of a lifted wall with the lower end 15 cm above the floor level. The suspended wall was subsequently lowered to the floor level to form a boundary continuous with the peripheral arena walls.

Finally, in a distinct set of experiments, object-vector cells were recorded in complete darkness to test for the effect of visual object cues. The mice first explored the arena with an object present and curtains fully enclosing the arena. Subsequently, the lights were turned off and the mouse explored the arena and the object in full darkness. The mouse was not taken out of the arena between the light and dark trials. Each trial lasted approximately 15 min.

Recording procedure. Data collection started 1–2 weeks after implantation of the tetrodes. During recording, the mouse was connected to an Axona data acquisition system (Axona) via an AC-coupled unity-gain operational amplifier close to the mouse's head, using a lightweight counterbalanced multiwire cable from both implants to an amplifier. Unit activity was amplified 3,000–14,000 times and band-pass filtered between 0.8 and 6.7 kHz. Triggered spikes were stored to disk at 48 kHz with a 32-bit time stamp. An overhead camera recorded the position of two light-emitting diodes (LEDs) on the head stage, each at a sampling rate of 50 Hz. The diodes were separated by 3 cm. To sample activity at multiple dorso-ventral MEC positions, the tetrodes were lowered in steps of 25–50 µm between trial sequences after all relevant tests had been completed. Recordings started as soon as the tetrodes were judged to be in the MEC, using theta modulation and presence of spatially or directionally modulated cells as criteria in addition to tetrode depth. **Spike sorting and cell classification.** Spike sorting was performed offline using graphical cluster-cutting software (tint, N.Burgess and Axona; or ctools, T. Waaga). Spikes were clustered manually in 2D projections of the multidimensional parameter space (consisting of waveform amplitudes), using autocorrelation and cross-correlation functions as additional separation tools and separation criteria. Cluster separation was assessed by calculating distances between spikes of different cells in Mahalanobis space³¹ (Extended Data Fig. 5). Noise in the vicinity of clusters was expressed as the *L* ratio³¹ (Extended Data Fig. 5). Clusters on successive recording trials were identified as the same unit if the locations of the spike clusters in cluster space were stable.

Firing rate maps and head-direction tuning curves. Position estimates were convolved with a 35-point Gaussian window and *x*, *y*-coordinates were sorted into 2 cm × 2-cm bins. Spike timestamps were matched with position timestamps. Only spikes collected at instantaneous running speeds above 3 cm/s were included. Firing rate distributions were determined by counting the number of spikes and assessing time spent in 2 cm × 2-cm bins of the firing rate maps and in directional bins of 5° in tuning curves for head direction. The distributions were subsequently smoothed with a 2D Gaussian kernel with s.d. of 2 bins (4 cm) in both the *x* and the *y* direction for the rate maps and with a Gaussian filter with an s.d. of 2 bins (10°) for the head-direction maps.

Firing fields in the rate map were detected by iteratively applying the Matlab 'contour' function (Mathworks), starting from the cell's peak firing rate until it reached 2 × s.d. of the firing rates of all bins in the rate map. Firing fields were defined as contiguous areas within a contour of at least 16 bins and with a peak firing rate of at least 2 Hz.

Spatial information content and spatial coherence. Information content was determined for each rate map by computing the spatial information rate³² as

$$\sum_{i=1}^N P_i \frac{\lambda_i}{\lambda} \log_2 \left(\frac{\lambda_i}{\lambda} \right)$$

in which λ_i is the mean firing rate in the *i*th bin, λ is the overall mean firing rate and P_i is the probability of the mouse being in the *i*th bin (occupancy in the *i*th bin/total recording time). Spatial information in bits per spike was obtained by dividing the information rate by the mean firing rate of the cell. Spatial coherence was calculated for each cell as the *z*-transform of the correlation between the firing rates of each bin and the averaged firing rates of the eight nearest neighbours of that bin.

Shuffling of spike data. To determine cutoff values for vector-map correlations, egocentric directionality, grid scores, head-direction scores, border scores and information content, a shuffling procedure was implemented. Shuffling of experimental data was conducted with 200 permutations for each cell. For each permutation, the entire sequence of spikes fired by the cell was time-shifted along the mouse's path

by a random interval between on one side 20 s and, on the other side, 20 s less than the length of the session, with the end of the session wrapped to the beginning. Time shifts varied randomly between permutations and between cells. Vector-map correlations, egocentric directionality, grid scores, head-direction scores, border scores and information content were calculated for each permutation and distributions of scores were plotted. For object-vector cells, the object location on the first object trial was used as the reference for vector maps in all permutations.

Definition of object-vector cells. Cells that, after insertion of the object, expressed new firing fields were selected for analysis. We distinguished between cells that fired at the object (object cells; field centre 0–4 cm from the centre of the object) and cells the firing fields (centres of mass) of which were offset by more than 4 cm from the object. The focus of the analyses was on the latter category, which accounted for nearly all object-responsive cells.

For cells with fields that were offset by more than 4 cm from the object centre, the vector-relationship between the cell's spatial firing and the object was expressed in a 'vector-map' in which firing rate (colour) was expressed as a function of distance (x) and direction (y) from the object centre (Fig. 1b). With the centre of the object as the reference, the arena was divided into directional bins of 5° width, and for each directional bin, the time-normalized firing rate was measured in distance bins of 2 cm (Fig. 1b). The resulting distance-by-direction matrix was smoothed with a 2D Gaussian kernel using a s.d. of 2 bins (10°, 4 cm). In the vector map, 0° was defined as east of the object in the room frame (Fig. 1a). The vector map of the object trial was then compared with that of the subsequent trial, for which the object was moved to a new location. Object-vector cells were defined as cells that had a correlation between vector maps on object and displaced-object trials that exceeded chance levels determined by repeated shuffling of the experimental data (see above). The 99th percentile correlation of the distribution of all vector-map correlations between shuffled object and displaced-object trials was taken to be the chance level. For a cell to be considered as an object-vector cell, spatial information on the object trial further had to exceed the 95th percentile for spatial information in the shuffled data, and the peak firing rate had to be at least 2 Hz. Vector maps for the no-object trial were made using the respective object location on the object trial as reference. Reducing the level of smoothing by 50% (kernel with s.d. of 1 bin) changed the number of object-vector cells by only one cell.

Vector maps were also used to determine the similarities of responses to different objects in experiments for which multiple objects were present in the arena. For each cell, we constructed vector maps around each object and compared these for different pairs of simultaneously presented objects. We then found the two fields in the pair of maps that had the nearest centre-to-centre distance and measured the difference in distance and orientation from the centre of the object.

Egocentric directional tuning. Egocentric directional tuning curves were constructed as described²⁴. In brief, tuning curves were constructed with movement (heading) direction bins of 20° relative to the object location, and with 0° defined as moving towards the object and ±180° moving away from the object. Curves were smoothed over 1.5 bins (30°) with a Gaussian filter. We defined the egocentric directionality index as the mean vector length of the tuning curve. Again, we defined a 99th percentile threshold by shuffling of the experimental data (see above).

Modelling of object-vector fields. We modelled firing rate as a function of distance, $d(x,y)$, from the preferred object vector using the general function:

$$f(\mathbf{d}) = a \exp[-\mathbf{d}^T \cdot \mathbf{A} \mathbf{d}] + b$$

in which \mathbf{d} is the Euclidian distance from the preferred vector, a is the amplitude, \mathbf{A} is a diagonal matrix and b is a constant. \mathbf{A} was multiplied by a rotation matrix, \mathbf{R} , to accommodate potential tilts of the firing fields.

More specifically, we let $\mathbf{A} \rightarrow \mathbf{R}^T \mathbf{A} \mathbf{R}$, with

$$\mathbf{R} = \begin{bmatrix} \cos(\theta) & \sin(\theta) \\ -\sin(\theta) & \cos(\theta) \end{bmatrix}$$

Model fitting was performed on the unsmoothed firing rate maps of object-vector cells (2.5-cm bin width) using the Matlab lsqcurvefit function. Initial guesses were based on vectors in Fig. 1e. For a circular Gaussian model:

$$\mathbf{A} = \begin{bmatrix} 1/2\sigma^2 & 0 \\ 0 & 1/2\sigma^2 \end{bmatrix}$$

And for an elliptic model:

$$\mathbf{A} = \begin{bmatrix} 1/2\sigma_x^2 & 0 \\ 0 & 1/2\sigma_y^2 \end{bmatrix}$$

in which σ_x and σ_y denote the different values of the s.d. in two dimensions.

We assessed the relative goodness of fit, F , for the circular and the elliptic models as

$$F = \frac{\mathbf{Z}_c - \mathbf{z} - \mathbf{Z}_e - \mathbf{z}}{\mathbf{z}}$$

in which \mathbf{Z}_c and \mathbf{Z}_e are the fitted surfaces of the circular and elliptic model, respectively, and \mathbf{z} is the unsmoothed firing rate map. A positive value for F indicates a better fit using the elliptic model. Multiplying F by 100 yields the percentage of the underlying data explained by the elliptic model as compared to the circular one. The analysis was limited to object-vector cells expressing only one object-vector field.

Analysis of parametric experiments. In experiments in which objects were elongated along one dimension, we applied a filtering procedure to distinguish object-vector responses from temporary random suprathreshold activity. For every detected field in every trial, we identified the vector between the centre-of-mass of the field and every point on the elongated object. This set of vectors was then compared with the original object-vector (the vector between the more point-like object and the field that moved with the object on the standard trials). If the magnitude of the vector difference between the original object vector and any of the vectors in the set of vectors between the field and any point on the elongated object was equal to or less than a length of five bins, the field was included in the analysis of field width. Similarly, in experiments with increasing object diameter or object height, only fields for which the magnitude of the vector difference compared to the original object vector was equal to or less than five bins were counted as object-vector fields and included in analyses of field size. Including all suprathreshold activity anywhere in the environment made no difference to the outcome of statistical tests, except in the elongation experiment, for which field widths as a function of the length of the object did not come out as significantly different when all suprathreshold activity was included. Vector tuning along the axis of the internal wall-like rectangular object was assessed by finding the locations on the internal wall from which the vector to the peak of a firing field was most similar to the object vector when the same cell was recorded in the presence of the smallest (6.75-cm wide) object (similarity was defined by the magnitude of the vector differences).

Definition of grid cells. The spatial periodicity of each rate map—the cell's grid score—was determined by calculating a spatial autocorrelogram^{22,33}. For each cell, a grid score was determined by taking a central circular sample of the autocorrelogram, with the central peak excluded (the central peak was defined as 100 or more contiguous pixels of $1.5 \times 1.5 \text{ cm}^2$ above a fixed threshold of $r > 0.1$), and comparing rotated versions of this sample^{22,33}. The Pearson correlation of the circular sample with its rotation in α° was obtained separately for angles of 60° and 120° on one hand and 30°, 90° and 150° on the other. The cell's grid score was defined as the minimum difference between any of the elements in the first group (60° and 120°) and any of the elements in the second.

A cell was defined as a grid cell if its grid score exceeded a chance level determined by repeated shuffling of the experimental data. If the grid score from the recorded data was larger than the 99th percentile of grid scores in the distribution of shuffled data from all cells, the cell was defined as a grid cell. As an additional criterion, we required the cell to have a peak firing rate of at least 2 Hz and a spatial information content exceeding the 95th percentile value of information content obtained from shuffled data.

Template grid patterns from object-vector cells with multiple fields. For cells with two or more object-vector fields, we constructed a regular grid lattice extrapolated from the positions of the two object-vector fields (Extended Data Fig. 4e). Template fields were modelled as circular areas centred at vertices in the grid lattice, and with size equal to the mean area of the two object-vector fields. A Z-score was calculated by first determining the difference between the mean firing rate inside the extrapolated template areas and the mean firing rate outside all projected and real firing fields, and then dividing this difference by the s.d. of the firing rate of all bins in the rate map.

Analysis of head-direction cells. The mouse's head direction was determined for each tracked sample by plotting the relative positions of the two LEDs onto the horizontal plane. The directional tuning function for each cell was obtained by plotting the firing rate as a function of the mouse's heading direction, divided into bins of 5° and smoothed with a Gaussian moving average of 2 bins on each side. Directional tuning was estimated by computing the length of the mean resultant vector (mean vector length) for the circular distribution of firing rates. For a cell to be included as a head-direction cell, its mean vector length needed to pass the 99th percentile threshold of the mean vector length in the shuffled version of the same data. In addition, peak directional tuning had to be at least 2 Hz and within trial stability (correlation) at least 0.50.

Analysis of border cells. Border cells were identified by computing a border score for each cell⁶. The cell's border score was expressed as the difference between the maximal length of a wall touching on any single firing field of the cell and the

average distance of the field (across pixels) from the nearest wall, divided by the sum of those values. Border scores thus ranged from -1 to $+1$. For circular arenas, the rate map was first transformed into a square image using a polar transform with the centre of the box as the reference. The resulting polar image represented distance from the wall (in centimetres) on one axis and distance along the perimeter or the wall (in degrees) on the other. The border score was then computed as for square arenas. As border cells often cover half of the arena in a circular environment, a border score of $+1$ would be assigned to cells with infinitely narrow fields lining up along the wall of half the box or covering 180° in the polar image. After border scores were computed for each cell, border cells were identified as cells in which the border score exceeded the 99th percentile of the distribution of border scores in shuffled versions of the same data. In addition, for a cell to be defined as a border cell, we required the cell to have a peak rate of at least 2 Hz and a spatial information content that exceeded the 95th percentile for spatial information on the no-object trial.

Boundary-vector cells in open environments. On open-arena trials, putative boundary-vector cells were identified using the following three criteria: (1) the spatial information content of the cell must exceed the 95th percentile for information content obtained from shuffled data; (2) the cell must have a firing field with a long axis of at least 70% of the length of any of the walls of the box, at any distance away from the wall; and (3) the long axis of the firing must be parallel to any of the walls of the box. We measured the degree to which a field was parallel to a wall by taking the angle between the wall and the regression line along the long axis of the firing field. If the angle between the regression line and the wall was equal to or less than 10° , and the coefficient of determination of the regression line was at least 0.1, the field was regarded as parallel to the wall.

Coherence between directional rate distributions. We quantified the degree to which orientation of different cell types shifted coherently between trials in different rooms by performing circular cross-correlations on their directional firing rate distributions. For each head-direction cell, we cross-correlated directional tuning curves obtained from the two recording rooms, using a bin size of 2° . For object-vector cells, we cross-correlated the object-centred allocentric directional tuning curves—in which firing rate was expressed as a function of orientation relative to object—across trials in the same two rooms, also using a bin size of 2° . For grid cells, we rotated the rate map in the first room in steps of 2° and correlated this map with the rate map of the other room for each step. For all cell types, we identified the rotational shift between the two pairs of distributions or maps that gave the peak correlation. We compared the distribution

of these differences with the distribution of pairwise differences obtained by randomly rotating the tuning curves while maintaining the shapes of the tuning curves. The maximum absolute difference in rotational shift between pairs is 180° . The expected mean and median values of a distribution of rotational shifts in which tuning curves have been randomly shifted is thus 90° for large sample sizes.

Histology and reconstruction of recording positions. The tetrodes were not moved after the final recording session. The mouse was given an overdose of pentobarbital and was perfused intracardially with 9% saline and 4% formaldehyde. The brain was extracted and stored in 4% formaldehyde. Frozen, 30-mm sagittal sections were cut, mounted on glass, and stained with cresyl violet (Nissl). The final position of the tip of each tetrode was identified on photomicrographs obtained with an Axio Scan.Z1 microscope and Axio Vision software (Carl Zeiss) (Extended Data Fig. 1).

Statistical tests. All statistical tests were two-sided. We used Mann–Whitney *U* tests for independent group comparisons and Wilcoxon signed-rank tests for paired tests. Correlations were determined using Pearson's product-moment correlation coefficients. Kruskall–Wallis test was used for variance analysis. No statistical methods were used to pre-determine sample sizes but our sample sizes are similar to those reported in previous publications. The study contained no randomization to experimental treatments and no blinding.

Reporting summary. Further information on research design is available in the Nature Research Reporting Summary linked to this paper.

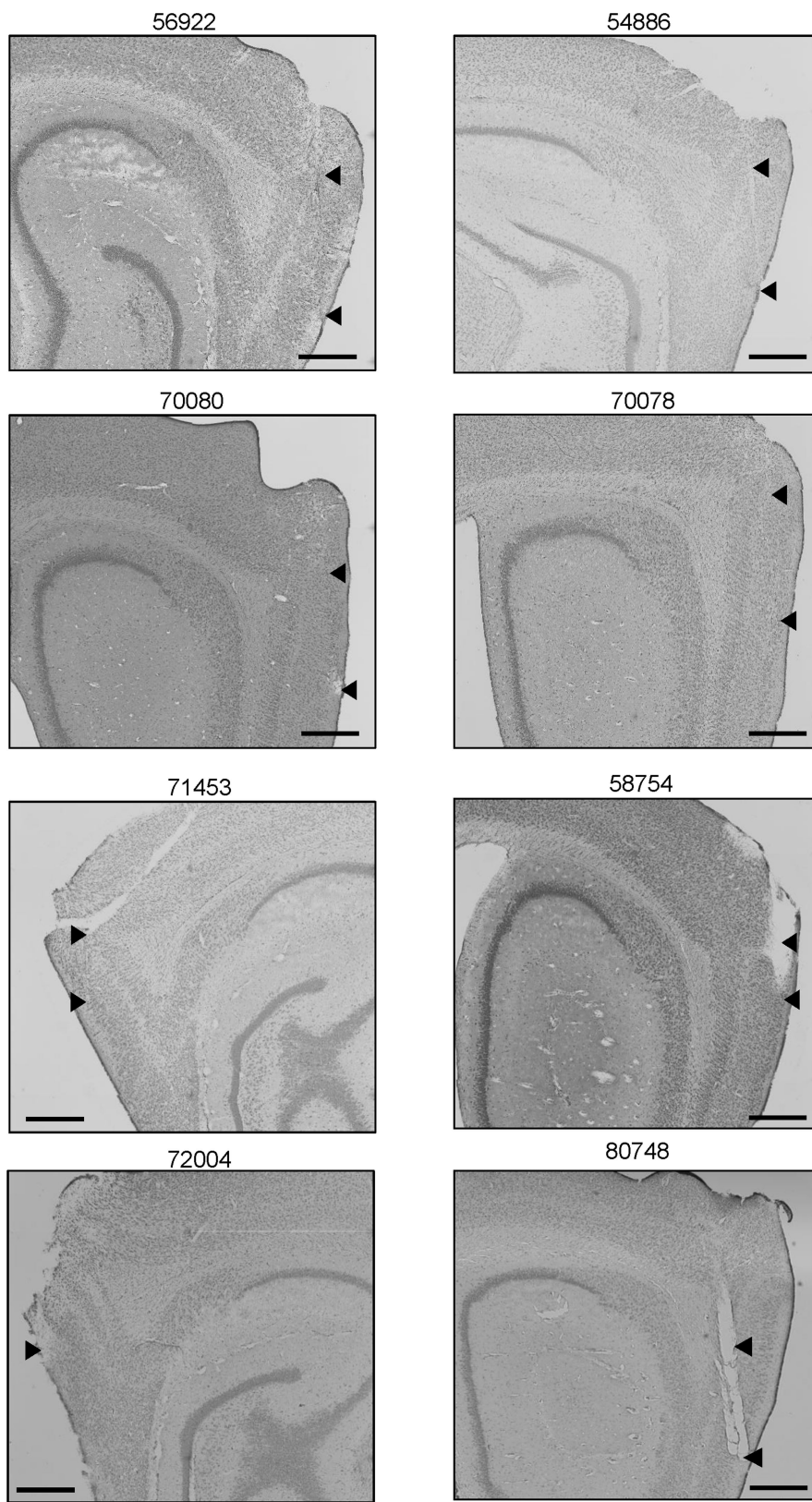
Data availability

Data sets supporting the findings of this paper are available on request from the corresponding authors.

Code availability

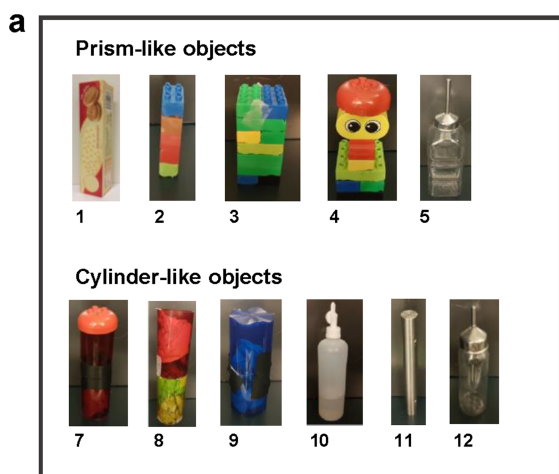
Custom code is available from the corresponding authors on request.

31. Schmitzer-Torbert, N., Jackson, J., Henze, D., Harris, K. & Redish, A. D. Quantitative measures of cluster quality for use in extracellular recordings. *Neuroscience* **131**, 1–11 (2005).
32. Skaggs, W. E., McNaughton, B. L., Gothard, K. M. & Markus, E. J. in *Advances in Neural Information Processing Systems 5* (eds. Hanson, S. J., Cowan, J. D. & Giles, C. L.) 1030–1037 (Morgan Kaufmann, 1993).
33. Langston, R. F. et al. Development of the spatial representation system in the rat. *Science* **328**, 1576–1580 (2010).



Extended Data Fig. 1 | Recording locations in the MEC. Representative examples of Nissl-stained sagittal brain sections showing tetrode locations for 8 of the 16 mice used for experiments. Mouse identifier (ID) numbers

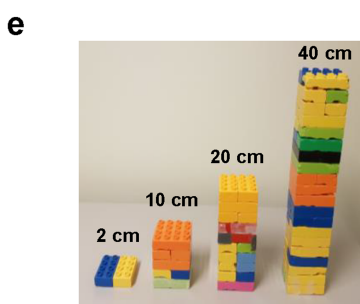
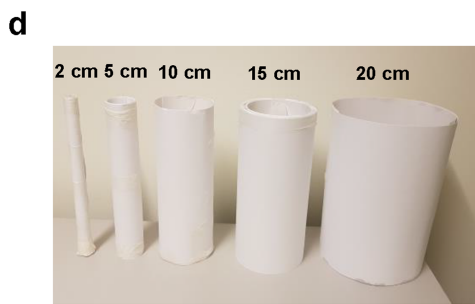
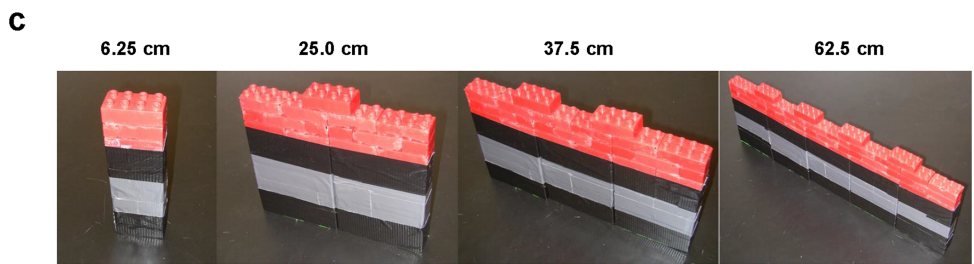
are indicated above each section. Pairs of black arrowheads indicate the dorsoventral range of the recording locations. Scale bar, 250 μ m.



b

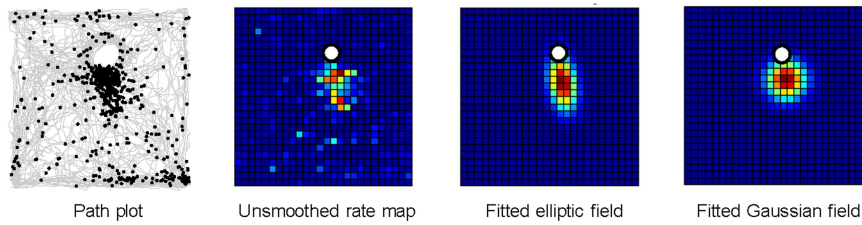
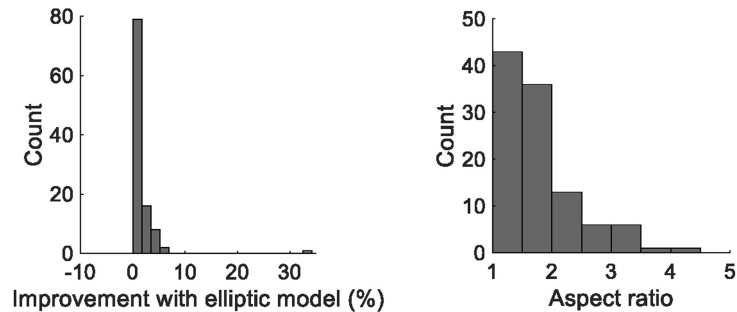
Prism-like objects	1	2	3	4	5
Dimensions (Height x width x length)	20 x 5.5 x 5.5 cm	9 x 3 x 3 cm	14 x 6.5 x 6.5 cm	16 x 6 x 6 (at base)	15 x 7 x 7 cm
Fabric	Paper	Hard plastic	Hard plastic	Hard plastic	Plastic

Cylinder-like objects	7	8	9	10	11	12
Dimensions (Height x diameter)	20 x 5.5 cm	30 x 8 cm	29 x 7 cm	20 x 8 cm	3 x 35 cm	13 x 5 cm
Fabric	Hard plastic/tape	Hard plastic	Soft plastic	Hard plastic	Metal	Plastic



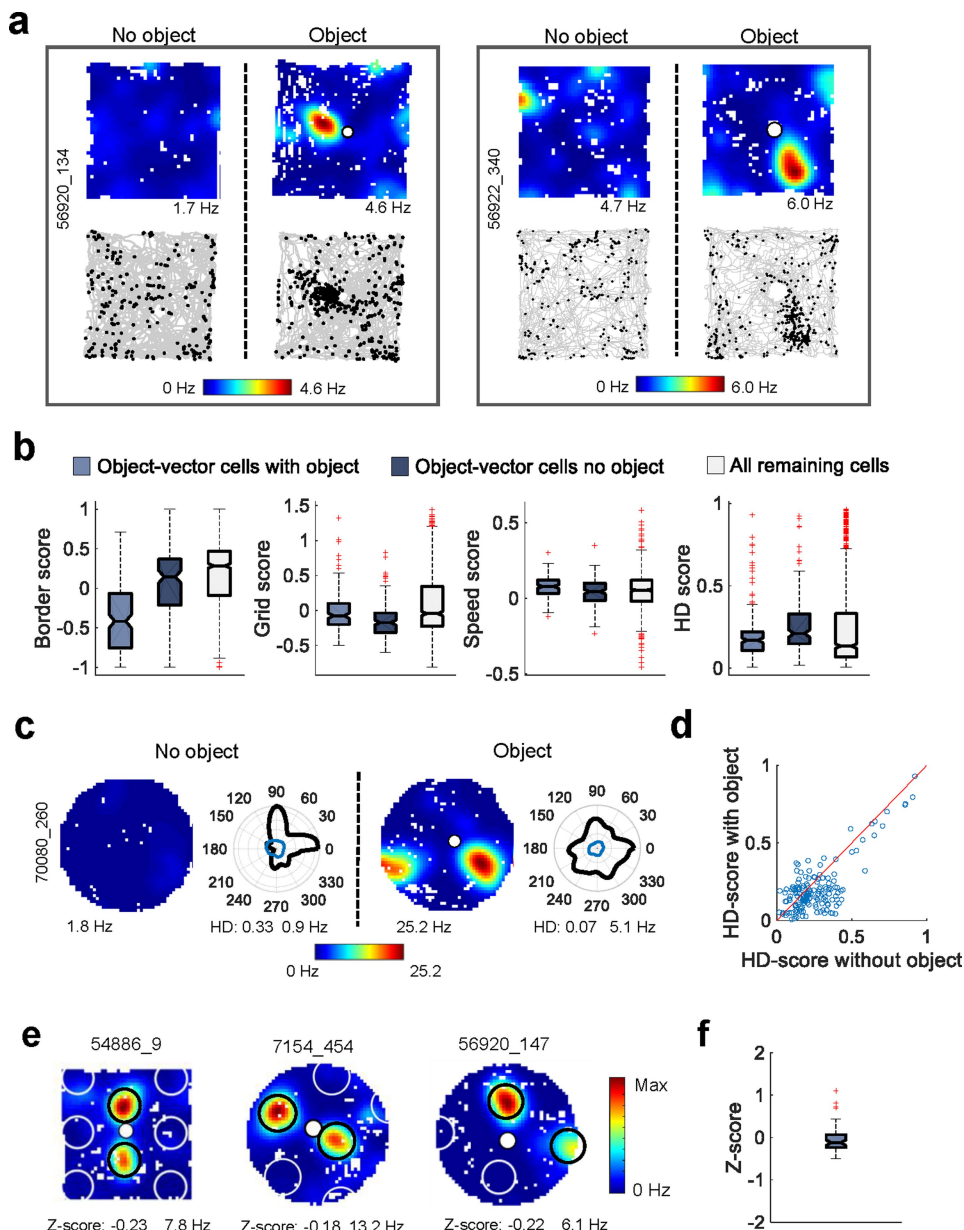
Extended Data Fig. 2 | List of all objects used to identify object-vector cells. **a**, All objects used in experiments with object-vector cells. Objects had either a prism-like or cylinder-like appearance, with some modifications, and varied in height and width. **b**, Shape, dimensions, colour and material of each object, numbered as in **a**. **c**, Prismatic objects of increasing length used for experiment in which a point-like prism tower

was changed across trials into a lengthy wall. Objects consisted of 21-cm-high, 3-cm-wide towers of Duplo Lego bricks with lengths of 6.75 cm, 25 cm, 37.5 cm and 62.5 cm. **d**, Cardboard cylinders of increasing diameter (2 cm, 5 cm, 10 cm, 15 cm and 20 cm). **e**, Prismatic Duplo Lego objects of increasing height (2 cm, 10 cm, 20 cm and 40 cm).

a**b**

Extended Data Fig. 3 | Ellipticity of object-vector fields. To more formally characterize the firing of object-vector cells, we compared two models of vector-determined firing, with firing fields corresponding to a Gaussian circle or an ellipse. The models were applied to the raw, unsmoothed firing rate maps. **a**, A slightly better fit is usually obtained from the elliptic model. Left to right: (1) path plot of an object-vector cell; (2) unsmoothed firing rate map of the cell; (3) object-vector field obtained by fitting an elliptic model to the raw unsmoothed firing rate map of the cell; and (4) object-vector field obtained by fitting a Gaussian model to

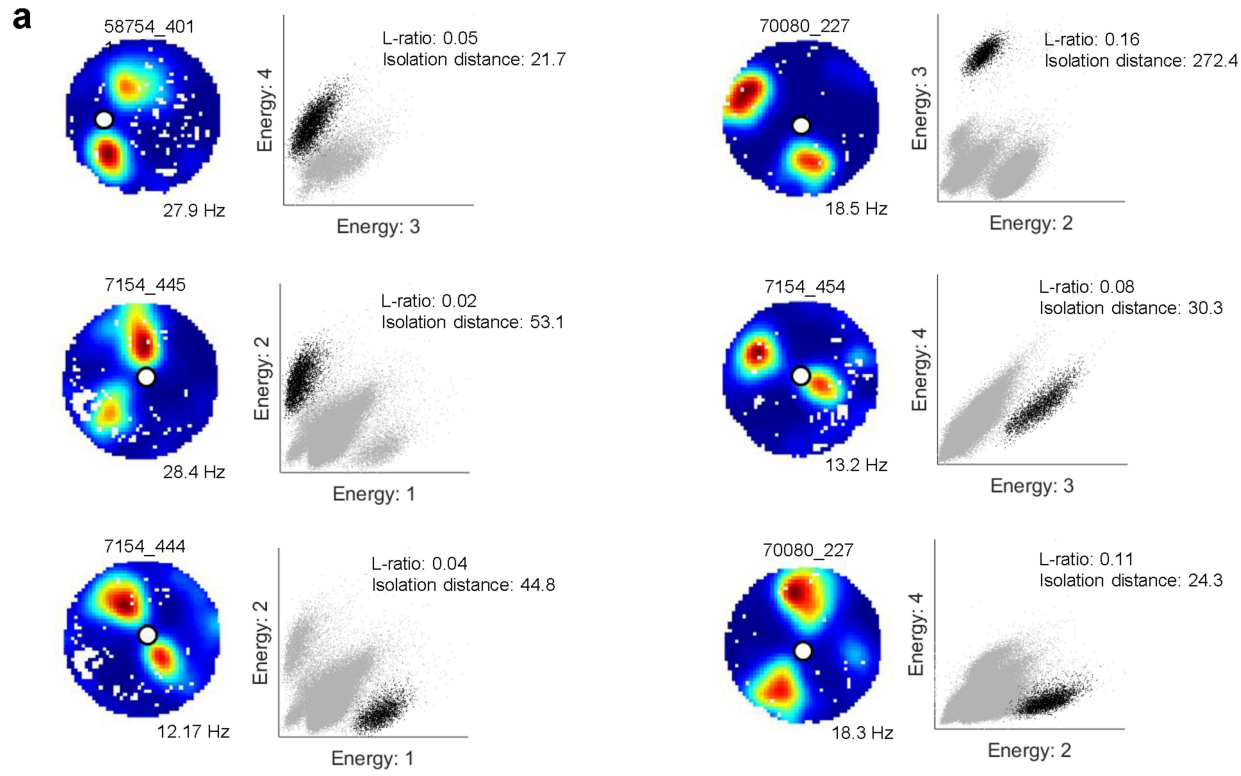
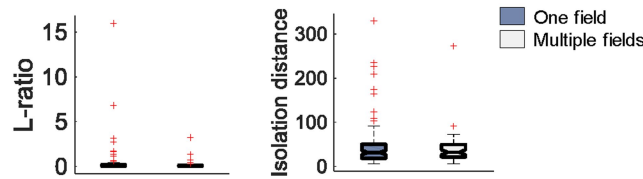
the raw unsmoothed firing rate map. For this cell, the elliptic fit explained 3.2% more of the underlying data (the unsmoothed firing rate map) than the Gaussian circle model. **b**, Left, frequency distributions showing relative goodness of fit (see Methods) of the elliptic and circular models. Right, aspect ratio (ratios between s.d. values in two dimensions) for all object-vector cells. Aspect ratios for the best fit had a median of 1.6 and 25th–75th percentiles of 1.3–2.0. An aspect ratio near 1 indicates that the firing field is almost circular.



Extended Data Fig. 4 | See next page for caption.

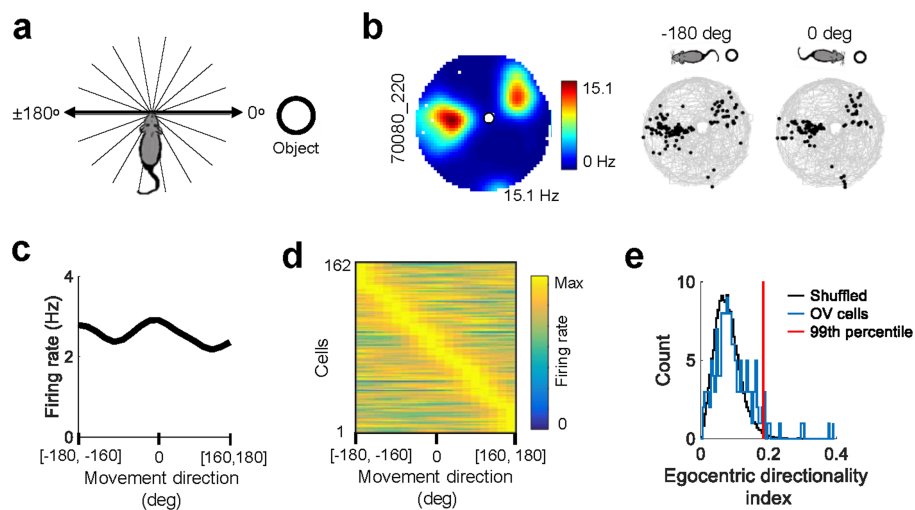
Extended Data Fig. 4 | Object-vector cells are distinct from other spatially modulated cell classes. **a**, Colour-coded rate maps (top) and path plots (bottom) for two representative object-vector cells recorded first without an object and then with an object (white circle). Path plots show the mouse's trajectory with spike locations superimposed as black dots. Peak rates, and mouse and cell ID numbers, are indicated (horizontal and vertical text labels, respectively). The cells responded vigorously to objects but did not have border or grid fields. In the no-object condition, 15 of 162 object-vector cells also passed the border cell criteria and 4 passed the criteria for grid cells. Lowering the minimum threshold for peak firing rate from 2 Hz to 1.5 Hz made no discernible difference: 163 cells passed the criteria for object-vector cells, and 18 of these cells passed the border cell criteria and 4 cells the grid cell criteria. **b**, Distribution of border scores, grid scores, speed scores, and head-direction scores for object-vector cells on trials without an object (dark blue boxes, $n = 162$), for object-vector cells on trials with an object (light blue boxes, $n = 162$), and for cells that did not satisfy criteria for object-vector cells on the no-object trial, including all other types of spatially or directionally modulated cells (light grey boxes, $n = 938$). Without objects present, border scores were higher in the overall population than in object-vector cells (Mann–Whitney U -test, $U = 5.7 \times 10^4$, $P = 0.0002$). Grid scores were also higher in the overall population than in object-vector cells (Mann–Whitney U -test, $U = 6.2 \times 10^4$, $P = 1.1 \times 10^{-10}$). By contrast, head-direction scores were higher for object-vector cells than for the remaining cells when objects were not present (Mann–Whitney U -test, $U = 1.1 \times 10^5$, $P = 1.6 \times 10^{-7}$), which suggests that a subset of object-vector cells is modulated by head-direction input. Head-direction tuning of object-vector cells decreased significantly when objects were present (Wilcoxon signed rank test, $W = 10,206$, $P = 1.7 \times 10^{-9}$) and was then not different from that of the overall population (Mann–Whitney U -test, $U = 93,560$, $P = 0.24$). Speed scores were not different for object-vector cells compared to the remaining cells (Mann–Whitney U -test, $U = 8.4 \times 10^4$, $P = 0.18$). All statistical tests were two-sided. Black line between box edges indicates median, box edges

indicate 25th and 75th percentiles, whiskers extend to the most extreme point that lies within $1.5 \times$ interquartile range (IQR), and data points larger than $1.5 \times$ IQR are considered outliers (red crosses). **c**, Response to object in an object-vector cell with significant tuning to head direction of the mouse. Left, recording with no object; right, with an object. For each trial, a colour-coded firing rate map is shown with a circular plot for firing rate as a function of head direction (black curve, firing rate; blue curve, time spent; HD, head-direction score (that is, mean vector length)). Peak rates are indicated for rate maps and directional tuning plots. The dispersed directional tuning on the baseline trial is typical; most direction-tuned object-vector cells had wide or multipeaked tuning curves (unlike those of ‘classical’ head-direction cells⁸). Note that this weak head-direction tuning is reduced when the object is introduced. **d**, Head-direction score for all object-vector cells that passed the head-direction criteria on the no-object trial, plotted against the head-direction score of the same cells on the object trial. Note the general reduction in head-direction tuning when the object is present. **e**, Colour-coded rate maps for three object-vector cells with two object-vector fields. Object-vector fields are indicated by black open circles. Small filled white circles represent objects. Large white and open circles indicate template areas in a regular grid lattice extrapolated from the positions of the two object-vector fields. A grid-pattern Z-score was calculated by first determining the difference between the mean firing rate inside the extrapolated areas (large white and open circles) and the mean firing rate outside all projected and real firing fields, and then dividing this difference by the s.d. of the firing rate. Z-scores and peak firing rates are indicated below each example map. Mouse and cell ID numbers are indicated at the top. **f**, Grid-pattern Z-scores, calculated as in **e**, for the entire population of object-vector cells with multiple object-vector fields ($n = 56$ cells). Box plot as in **b**. Fluctuation of Z-scores around 0 (median -0.12 , 25th–75th percentiles -0.24 to 0.07) suggests that the two (or three) fields of the object-vector cells are not part of a regular grid pattern.

**b**

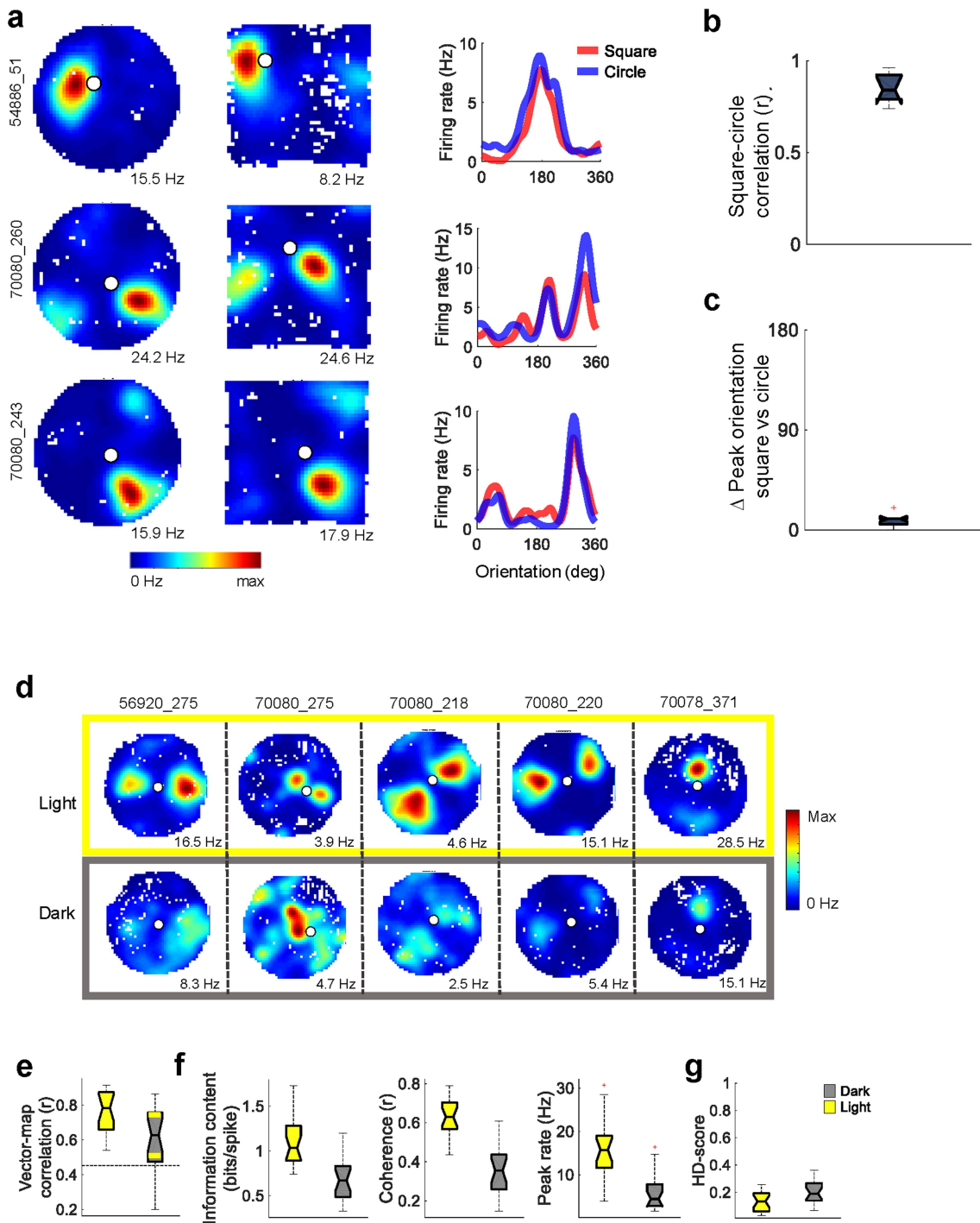
Extended Data Fig. 5 | Spike clusters of object-vector cells with two discrete firing fields. Separation of spikes from object-vector cells with two firing fields from spikes of other simultaneously recorded MEC cells. **a**, Examples of cell separation in 2D projections of multidimensional cluster diagrams. First and third columns, colour-coded rate maps showing two distinct object-vector cells, with mouse and cell ID numbers (top) and peak rates (bottom) indicated. Second and fourth columns, scatter plots showing relationship between energy (square of signal) for spikes recorded from two selected electrodes of a tetrode in the recording that contains the object-vector cell in the rate map to the left. The electrode numbers in each pair are indicated on axis labels. Each dot represents one sampled signal. Clusters are likely to correspond to spikes that originate from the same cell. The cluster giving rise to the rate

map to the left of each scatter plot is shown in black; remaining signals in grey. L -ratio and isolation distance³¹ for cluster in black are indicated above the scatter plot. Note clear separation of the object-vector cell from other spikes, which suggests that it is unlikely that second fields reflected contamination of spikes from other cells. **b**, Distribution of L -ratio and isolation distance for all object-vector cells with one field (dark blue boxes; $n = 102$ cells; median L -ratio 0.06 (25th–75th percentiles 0.02–0.19); median isolation distance 31.2 (18.0–49.7)), and all with two or three fields (light grey boxes; $n = 60$ cells; median L -ratio 0.06 (0.02–0.14); median isolation distance 31.7 (21.4–49.2)). Black line between box edges indicates median, box edges indicate 25th and 75th percentiles, whiskers extend to the most extreme point that lies within $1.5 \times$ IQR, and data points larger than $1.5 \times$ IQR are considered outliers (red crosses).



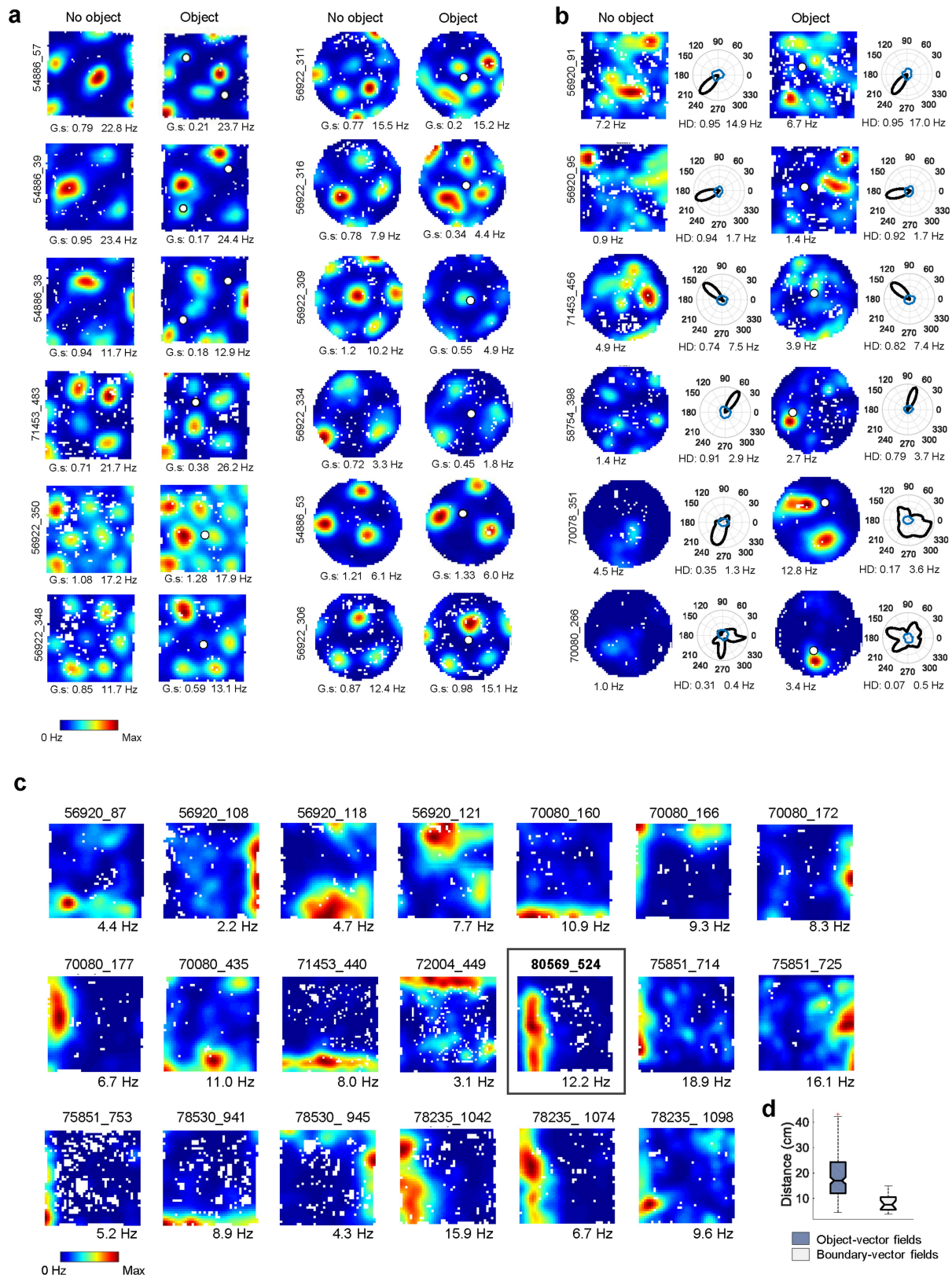
Extended Data Fig. 6 | Object-vector cells are allocentric. **a**, Egocentric reference frame with 0° defined as moving towards the object (white circle) and 180° as moving away from the object. **b**, Left, colour-coded firing rate map for a representative object-vector cell (peak rate below rate map; mouse and cell ID numbers indicated in vertical text bar). Right, path plot showing, for the same cell as in the rate map, the mouse's path with overlaid spike locations in black. Left path plot shows spikes on trajectories away from the object; right plot shows spikes on trajectories towards the object. **c**, Egocentric directional tuning curve for the cell in **b**. Firing rate is shown as a function of direction of movement relative to the object. Directional bins were 20° . Note that egocentric directional modulation is nearly absent. **d**, Colour-coded egocentric directional tuning curves (as in

c) for all object-vector cells. Each horizontal line corresponds to one cell and shows firing rate, colour-coded as a function of movement direction. Cells are sorted according to the movement direction that had the highest firing rate (light yellow). Note the relative absence of egocentric directional tuning. **e**, Distribution of egocentric directional modulation across the entire sample of object-vector cells. Egocentric directional modulation was estimated by defining for each cell an egocentric directionality index as the mean vector length of the egocentric tuning curve. Distribution of observed values for object-vector cells is shown in blue, shuffled data in grey. Red line marks the 99th percentile of egocentric directional modulation values for the shuffled data. Only ten object-vector cells had egocentric modulation that exceeded the 99th percentile.



Extended Data Fig. 7 | Orientation of object-vector fields is independent of the geometry of the environment but breaks down in the absence of visual input. **a–c**, Experiment in which eight cells from three mice were recorded successively in a circular and a square recording box. The boxes were placed at the same location in the recording room and cues external to the box were identical. **a**, Left, colour-coded rate maps of three cells recorded first in the circle, then in the square. Peak rates are indicated below the rate maps, mouse and cell ID numbers to the left. Colour bar indicates normalized firing rate. Right, directional tuning curves for the same three cells, with firing rates shown as a function of allocentric direction relative to the object. **b**, Correlation between directional tuning curves in square and circular environments for all eight cells. Black line between box edges indicates median, box edges indicate 25th and 75th percentiles, whiskers extend to the most extreme point that lies within $1.5 \times$ IQR. **c**, Difference in peak direction of tuning curves between square and circle for all eight cells. **d–f**, Object-vector fields recorded in light and in complete darkness. **d**, Colour-coded firing rate

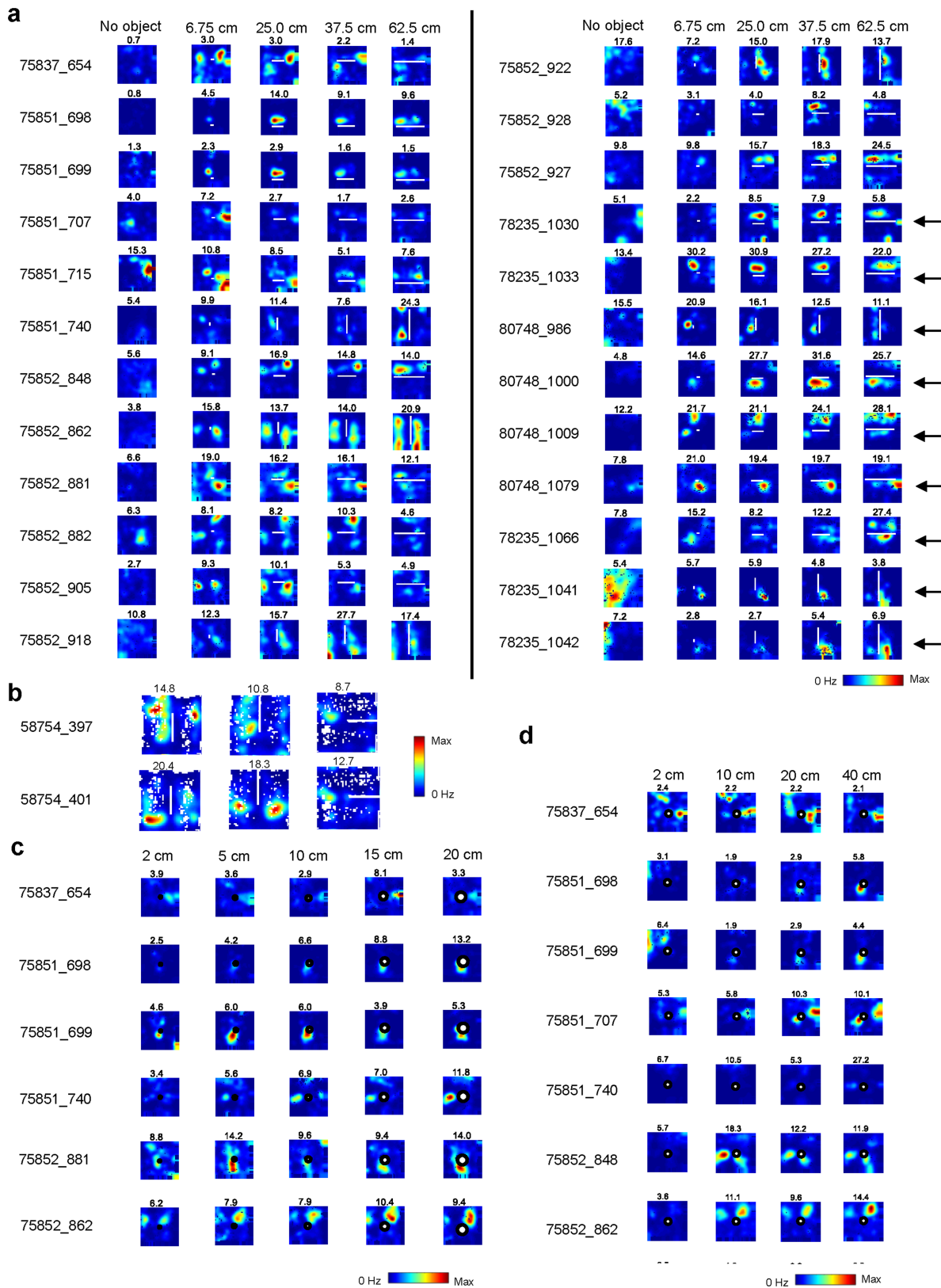
maps from five example cells recorded successively in light and darkness (top and bottom, respectively). Mouse and cell ID numbers are shown at the top of each column, peak rates below each rate map. Colour scale is similar for each column of rate maps. **e**, Distribution of vector-map correlations across pairs of trials recorded either successively in light (yellow) or first in light and then in darkness (grey; $n = 21$ cells). Stippled line marks the 99th percentile correlation threshold. **f**, Distributions of spatial information content, spatial coherence, peak firing rate and mean firing rate in light and in darkness. All four measures decreased from light to darkness (spatial information content: Wilcoxon signed-rank test, $W = 227$, $n = 21$, $P = 1.1 \times 10^{-4}$; spatial coherence: $W = 231$, $n = 21$, $P = 6.0 \times 10^{-5}$; peak firing rate: $W = 230$, $n = 21$, $P = 6.9 \times 10^{-5}$; mean firing rate: $W = 212$, $n1 = n2 = 95$, $P = 8.0 \times 10^{-4}$). All statistical tests were two-sided. **g**, Distribution of head-direction scores of all object-vector cells recorded in light and in darkness. Head-direction tuning increased significantly in the absence of visual cues (two-sided Wilcoxon signed rank test: $W = 36$, $n = 21$, $P = 0.005$).



Extended Data Fig. 8 | See next page for caption.

Extended Data Fig. 8 | Intersection with grid cells, head-direction cells and boundary-vector cells. **a**, Colour-coded rate maps showing 12 representative grid cells recorded in the absence (left) and presence (right) of objects on consecutive trials. Mouse and cell ID numbers are indicated to the left of each pair of columns; grid score (G.s.) and peak rate are shown below each rate map. Scale bar indicates firing rate. Cells in the top three rows of the left pair of columns are examples of grid cells that expressed an extra field in the vicinity of at least one of the objects. Such effects were observed in 10 out of 124 grid cells. Only four grid cells passed the criteria for object-vector cells. Grid fields from the no-object trial mostly retained their firing locations when the object was added, but in a few cases single fields were moderately displaced or the grid underwent mild disruption. **b**, Colour-coded rate maps and head-direction tuning curves for six representative head-direction cells recorded with no object (left) and with an object (right) on consecutive trials. Mouse and cell ID numbers are indicated to the left; peak rate is shown below each rate map and head-direction score and peak rate are shown below each head-direction tuning curve. Sharply tuned head-direction cells mostly failed to develop vector fields in the presence of objects (exemplified by the cells in the top three rows). One of the few object-vector cells that also had

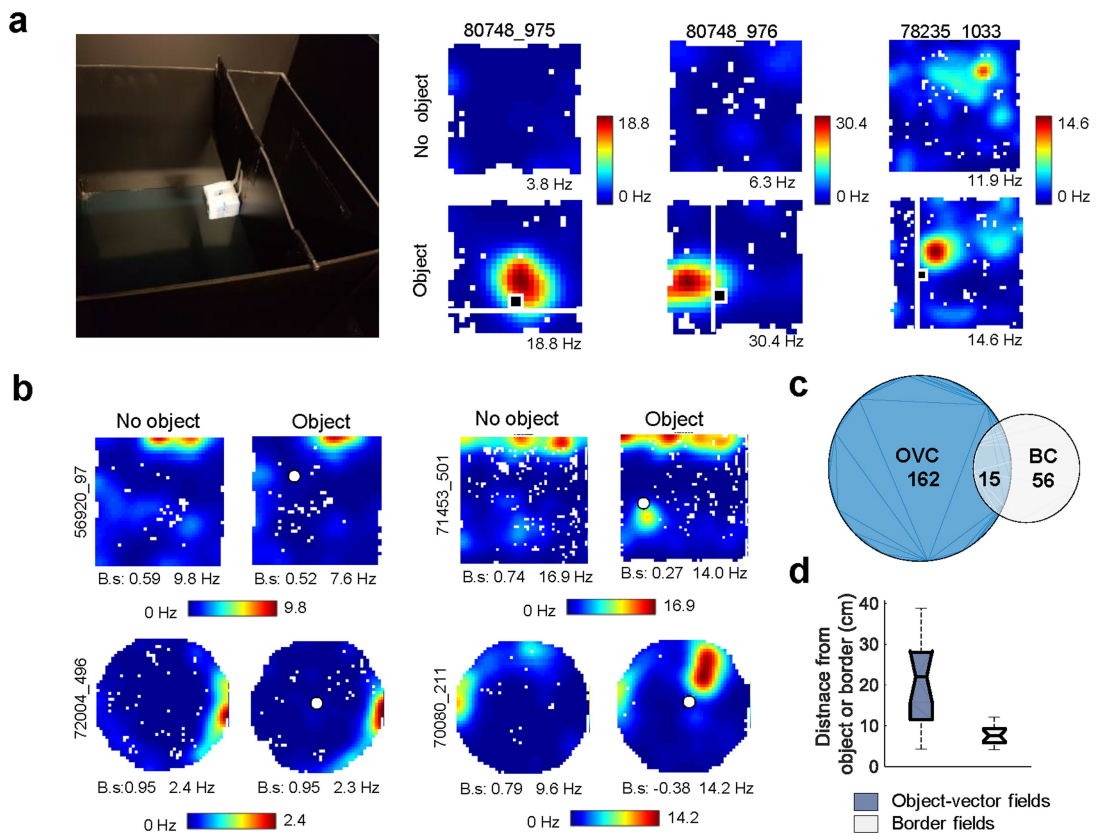
sharp head-direction tuning is cell 398 in the fourth row. The majority of object-vector cells that passed as head-direction cells had only moderate head-direction tuning, and this tuning was clearly reduced when the object was introduced (Extended Data Fig. 4c, d and exemplified by cells 351 and 266 in the two bottom rows of this panel). **c**, Colour-coded rate maps for all cells that pass a criterion for boundary-vector cells. Symbols as in **a**. Twenty out of 840 cells passed the criterion for boundary-vector cells. Among these, only one had a firing field that did not encroach upon the wall (mouse 80569, cell 524, highlighted in square frame). **d**, Distance between boundary and centre of boundary-vector firing field ($n = 20$ fields from 20 cells) for all cells that passed the criterion for boundary-vector cells, compared to distance between nearest point of object and centre of object-vector fields ($n = 221$ object-vector fields from 162 cells). Black line between box edges indicates median, box edges indicate 25th and 75th percentiles, whiskers extend to the most extreme point that lies within $1.5 \times \text{IQR}$, and data points larger than $1.5 \times \text{IQR}$ are considered outliers (red crosses). The distribution of distances in object-vector fields is skewed towards greater distances than the distribution of distances in boundary-vector fields (two-sided Mann–Whitney U -test, $U = 703$, $P = 9.0 \times 10^{-9}$).



Extended Data Fig. 9 | See next page for caption.

Extended Data Fig. 9 | Rate maps from all recordings with stepwise increases in length, diameter or height of the object. **a**, Colour-coded firing rate maps of all 24 cells recorded in experiments in which objects were elongated in one dimension. Each row of four rate maps shows one cell. The four maps are scaled to the same maximum rate (common colour scale). Mouse and cell ID numbers are indicated to the left of each row. Fifteen cells were recorded while the length of the object was increased in steps from 6.75 cm to 62.5 cm. Nine cells were recorded while the length of the object was changed in the opposite direction, from 62.5 cm to 6.75 cm (cells indicated by arrows to the right). For some cells (for example, cells 862 and 927), firing fields increased in length as the object was extended;

for other cells (for example, cells 1079 and 1042), the fields retain similar sizes and shapes across the entire spectrum of object lengths. **b**, Rate maps showing object-vector cell in experiment with no gap between internal and external walls (middle, right). **c**, Firing rate maps of 6 out of 23 cells recorded in experiments in which the diameter of a cylindrical object was increased from 2 cm to 20 cm. Note persistence of firing fields with increasing diameter of the object. Scale bar indicates colour-coded firing rate. **d**, Firing rate maps of 7 out of 21 cells recorded in experiments in which the height of prismatic object was increased from 2 cm to 40 cm. Colour-coded firing rate is indicated by scale bar.



Extended Data Fig. 10 | Distinction between object-vector cells and border cells. **a**, Experiment with object on suspended wall. Image to the left shows recording box with an object attached to a suspended wall with a 15-cm passage underneath the wall and the object. In this configuration, there is no impediment to the mouse's movement near the object. Right, colour-coded rate maps for three example object-vector cells recorded on trials without any objects present (top row) and with an object (black square) attached to a suspended wall (white line). The three cells respond robustly to the suspended object. **b**, Colour-coded firing rate maps of four border cells recorded in the absence or presence of an object. The two cells on the left (one in a square and one in a circular box) showed no response to the object. The two cells on the right produced clear object-vector fields. **c**, Overlap between populations of object-vector cells and

border cells (BCs). Fifteen out of 56 border cells also passed the criteria for object-vector cells. The two cells to the right in **b** are among those cells. **d**, Box plot showing, for the 15 overlapping border and object-vector cells, the distance from centres of object-vector fields to the nearest point of the object, and the distance from centres of border fields to the nearest wall. Black line between box edges indicates median, box edges indicate 25th and 75th percentiles, whiskers extend to the most extreme point that lies within $1.5 \times \text{IQR}$. Mean distance from object-vector field to object was significantly greater than the distance from border field to the wall (object-vector field to object: 21.4 ± 2.6 cm; border field to wall: 7.6 ± 0.6 cm; two-sided Mann–Whitney U -test, $U = 381$, $P = 1.6 \times 10^{-4}$), consistent with the interpretation that border cells and object-vector cells are functionally independent (Fig. 4).

Reporting Summary

Nature Research wishes to improve the reproducibility of the work that we publish. This form provides structure for consistency and transparency in reporting. For further information on Nature Research policies, see [Authors & Referees](#) and the [Editorial Policy Checklist](#).

Statistical parameters

When statistical analyses are reported, confirm that the following items are present in the relevant location (e.g. figure legend, table legend, main text, or Methods section).

n/a Confirmed

- The exact sample size (n) for each experimental group/condition, given as a discrete number and unit of measurement
- An indication of whether measurements were taken from distinct samples or whether the same sample was measured repeatedly
- The statistical test(s) used AND whether they are one- or two-sided
Only common tests should be described solely by name; describe more complex techniques in the Methods section.
- A description of all covariates tested
- A description of any assumptions or corrections, such as tests of normality and adjustment for multiple comparisons
- A full description of the statistics including central tendency (e.g. means) or other basic estimates (e.g. regression coefficient) AND variation (e.g. standard deviation) or associated estimates of uncertainty (e.g. confidence intervals)
- For null hypothesis testing, the test statistic (e.g. F , t , r) with confidence intervals, effect sizes, degrees of freedom and P value noted
Give P values as exact values whenever suitable.
- For Bayesian analysis, information on the choice of priors and Markov chain Monte Carlo settings
- For hierarchical and complex designs, identification of the appropriate level for tests and full reporting of outcomes
- Estimates of effect sizes (e.g. Cohen's d , Pearson's r), indicating how they were calculated
- Clearly defined error bars
State explicitly what error bars represent (e.g. SD, SE, CI)

Our web collection on [statistics for biologists](#) may be useful.

Software and code

Policy information about [availability of computer code](#)

Data collection

Data was collected using DacqUSB (Axona Ltd., Herts, U.K.). Axio Vision software (Carl Zeiss, Germany) for reconstruction of recording sites

Data analysis

Custom code written in MATLAB 2016b was used for analysis. Cluster cutting: Tint (Neil Burgess and Axona Ltd.), or ctools (Torgeir Waaga)

For manuscripts utilizing custom algorithms or software that are central to the research but not yet described in published literature, software must be made available to editors/reviewers upon request. We strongly encourage code deposition in a community repository (e.g. GitHub). See the Nature Research [guidelines for submitting code & software](#) for further information.

Data

Policy information about [availability of data](#)

All manuscripts must include a [data availability statement](#). This statement should provide the following information, where applicable:

- Accession codes, unique identifiers, or web links for publicly available datasets
- A list of figures that have associated raw data
- A description of any restrictions on data availability

"Data supporting the main findings is available on request." Accession codes/ identifiers will be provided in the final version. Applies to all figures.

Field-specific reporting

Please select the best fit for your research. If you are not sure, read the appropriate sections before making your selection.

Life sciences

Behavioural & social sciences

Ecological, evolutionary & environmental sciences

For a reference copy of the document with all sections, see nature.com/authors/policies/ReportingSummary-flat.pdf

Life sciences study design

All studies must disclose on these points even when the disclosure is negative.

Sample size Sample sizes were chosen based on previous studies.

Data exclusions Spike clusters were monitored over successive days to ensure the same cells were not included twice

Replication Results were replicated across subjects within each experiment. Results were also replicated by different experimenters.

Randomization Animals were not assigned to groups

Blinding Investigators were not blinded because the study had only one experimental group (treatments were within subjects)

Reporting for specific materials, systems and methods

Materials & experimental systems

n/a	Involved in the study
<input checked="" type="checkbox"/>	<input type="checkbox"/> Unique biological materials
<input checked="" type="checkbox"/>	<input type="checkbox"/> Antibodies
<input checked="" type="checkbox"/>	<input type="checkbox"/> Eukaryotic cell lines
<input checked="" type="checkbox"/>	<input type="checkbox"/> Palaeontology
<input type="checkbox"/>	<input checked="" type="checkbox"/> Animals and other organisms
<input checked="" type="checkbox"/>	<input type="checkbox"/> Human research participants

Methods

n/a	Involved in the study
<input checked="" type="checkbox"/>	<input type="checkbox"/> ChIP-seq
<input checked="" type="checkbox"/>	<input type="checkbox"/> Flow cytometry
<input checked="" type="checkbox"/>	<input type="checkbox"/> MRI-based neuroimaging

Animals and other organisms

Policy information about [studies involving animals](#); [ARRIVE guidelines](#) recommended for reporting animal research

Laboratory animals 16 male black 6 mice, 4-11 months old, were used

Wild animals The study did not involve wild animals

Field-collected samples The study did not involve field collected samples